

# THE WEAK LENSING SIGNAL AND THE CLUSTERING OF BOSS GALAXIES: COSMOLOGICAL CONSTRAINTS

SURHUD MORE<sup>1</sup>, HIRONAO MIYATAKE<sup>2,1</sup>, RACHEL MANDELBAUM<sup>3</sup>, MASAHIRO TAKADA<sup>1</sup>, DAVID. N. SPERGER<sup>2</sup>, JOEL R. BROWNSTEIN<sup>4</sup>, DONALD P. SCHNEIDER<sup>5,6</sup>

<sup>1</sup> Kavli Institute for the Physics and Mathematics of the Universe (WPI), TODIAS, The University of Tokyo, Chiba, 277-8583, Japan

<sup>2</sup> Department of Astrophysical Sciences, Princeton University, Peyton Hall, Princeton NJ 08544, USA

<sup>3</sup> McWilliams Center for Cosmology, Department of Physics, Carnegie Mellon University, Pittsburgh, PA 15213, USA

<sup>4</sup> Department of Physics and Astronomy, University of Utah, 115 S 1400 E, Salt Lake City, UT 84112, USA

<sup>5</sup> Department of Astronomy and Astrophysics, The Pennsylvania State University, University Park, PA 16802, USA

<sup>6</sup> Institute for Gravitation and the Cosmos, The Pennsylvania State University, University Park, PA 16802, USA

*To be submitted to the Astrophysical Journal*

## ABSTRACT

We perform a joint analysis of the abundance, the clustering and the galaxy-galaxy lensing signal of galaxies from Data Release 11 of the Sloan Digital Sky Survey III Baryon Oscillation Spectroscopic Survey. We fit halo occupation parameters and cosmological parameters ( $\Omega_m$  and  $\sigma_8$ ) to both of these observables simultaneously, and thus break the degeneracy between galaxy bias and cosmology. The cosmological analysis is the first of its kind to be performed at a redshift as high as 0.53. We present measurements of the clustering signal of galaxies by utilizing various stellar mass threshold samples. The galaxy-galaxy weak lensing signal is obtained by using the shape catalog of background galaxies from the Canada France Hawaii Telescope Legacy Survey, which was made publicly available by the CFHTLenS collaboration, with an area overlap of about 100 deg<sup>2</sup>. We analyze these measurements in the framework of the halo model. Adopting a flat  $\Lambda$ CDM cosmology with priors on  $\Omega_b h^2$ ,  $n_s$  and  $h$  from the analysis of WMAP 9-year data, we obtain  $\Omega_m = 0.310^{+0.019}_{-0.020}$  and  $\sigma_8 = 0.785^{+0.044}_{-0.044}$  (68% confidence) after marginalizing over the halo occupation distribution parameters and a number of other nuisance parameters in our model. We demonstrate the robustness of our results with respect to sample selection and a variety of systematics such as the halo off-centering effect and possible incompleteness in our sample. Our constraints are consistent, complementary and competitive with those obtained using other independent probes of these cosmological parameters.

*Subject headings:* cosmology: theory - methods: numerical - dark matter - galaxies: clusters: general

## 1. INTRODUCTION

The overwhelming majority of the energy density of the Universe today is dominated by two mysterious components – dark energy and cold dark matter – both motivated by astrophysical observations (see e.g., Ostriker et al. 1974; Rubin et al. 1978; Riess et al. 1998; Perlmutter et al. 1999; Hinshaw et al. 2013; Planck Collaboration et al. 2013a). Since their discovery, the field of observational cosmology has focused on characterizing the precise abundance, the statistical distribution and the phenomenological behaviour of these components. Geometrical probes such as the observations of type-Ia supernovae (see e.g., Lampeitl et al. 2010; Sullivan et al. 2011; Suzuki et al. 2012) and the baryonic acoustic oscillation measurements (see e.g., Eisenstein et al. 2005; Percival et al. 2007a; Blake et al. 2011a; Anderson et al. 2014) have provided constraints on the energy density of various components in the Universe as a function of redshift, but are insensitive to the statistical properties of the dark matter distribution. Probing the latter requires constraints on the growth of structure in the Universe, which can be provided by measurements of the abundance of galaxy clusters (see e.g., Vikhlinin et al. 2009; Mantz et al. 2010; Rozo et al. 2010; Benson et al. 2013; Haselfield et al. 2013; Planck Collaboration et al. 2013c), redshift space distortions (see e.g., Percival et al. 2004; Beutler et al. 2012; Reid et al. 2014) and the statistics of weak gravitational lensing as a function of redshift (see e.g., Van Waerbeke et al. 2000; Lin et al. 2012; Huff et al. 2014; Heymans et al. 2013; Mandelbaum et al. 2013). Over the next decade, a combination of these probes will enable a phenomenological

understanding of the nature of dark energy and dark matter as well as stringent constraints on modifications to gravity (see e.g., Albrecht et al. 2006).

The growth of structure in the Universe is driven by the growth of fluctuations in dark matter, which are easier to describe analytically on large scales (Bernardeau et al. 2002) or via collisionless numerical simulations on small scales (Davis et al. 1985) than the variety of astrophysical processes that baryons undergo in order to form galaxies (see e.g., Springel et al. 2005; Rudd et al. 2008; Vogelsberger et al. 2014). Observationally, however, it is easier to use galaxies to trace out the underlying structure in matter. Since galaxies form within halos, at the peaks of the matter density field, using galaxies as tracers produces a biased view of the matter distribution (Kaiser 1984). The bias of halos with respect to the matter distribution and its dependence on halo mass can be fortunately predicted given the cosmological parameters within the framework of the standard concordance cosmological model (Bardeen et al. 1986; Mo & White 1996a; Sheth & Tormen 1999; Sheth et al. 2001; Tinker et al. 2010).

On large scales the bias of halos and the galaxies that reside in them approaches a constant value. On such scales the shape of the matter two-point function (the power spectrum or the correlation function) can be inferred from the observed galaxy two-point function, and used to constrain cosmological parameters (Tegmark et al. 2004; Percival et al. 2007b; Reid et al. 2010). However, in the case of the galaxy two-point function, the amplitude of the matter power spectrum, which is essential to study the growth of structure, is entirely

degenerate with the value of the bias. The determination of galaxy bias can be complicated as it is known to depend upon the properties of galaxies such as their luminosity and colour (Norberg et al. 2001; Tegmark et al. 2004; Zehavi et al. 2011; Guo et al. 2013), and is quite scale dependent on small scales (Mann et al. 1998). Nevertheless, this degeneracy between the large scale bias and the amplitude of the matter power spectrum can be broken if there is a way to infer the connection between galaxies and their halo masses (Seljak et al. 2005).

There are a number of different approaches to directly infer the galaxy-dark matter connection. Many different observables can be used to probe this connection, including galactic rotation curves (Rubin 1983), kinematics of satellite galaxies (Zaritsky et al. 1997; van den Bosch et al. 2004; More et al. 2009b, 2011), small scale redshift space distortions (Li et al. 2012), X-ray emission from the hot intra-cluster medium (see reviews by Kravtsov & Borgani 2012; Etori et al. 2013). However, these methods assume that the system is in dynamical equilibrium, an assumption that is certainly violated in some systems. Weak gravitational lensing provides a way to circumvent this assumption and can be used as a relatively clean probe of the halo masses. In combination with weak lensing, the information encapsulated in the shape and amplitude of the clustering signal can be fully exploited (Seljak et al. 2005; Cacciato et al. 2009; Mandelbaum et al. 2013; Cacciato et al. 2013a; More et al. 2013; Reid et al. 2014). This combination can provide simultaneous constraints on the connection between galaxies and dark matter and the cosmological parameters. Cosmological constraints from such studies obtained at different cosmic epochs can then be used to constrain the equation of state of dark energy.

In this paper, we will measure the large scale clustering of galaxies in the Sloan Digital Sky Survey III (SDSS-III hereafter) Baryon Oscillation Spectroscopic Survey (BOSS hereafter) in order to determine the amplitude of the clustering signal. In particular, we will employ the CMASS galaxy sample from BOSS as our parent sample. We will use the deep but limited area imaging data from the Canada France Hawaii Telescope Legacy Survey (CFHTLS hereafter), to measure the weak gravitational lensing signal around galaxies from BOSS to calibrate the masses of the halos in which they reside. We will model these observations simultaneously in the framework of the halo model. This paper is second in the series of papers that discuss the results of our analysis. In Miyatake et al. (2013, Paper I hereafter), we discuss the astrophysical constraints from our analysis, focusing on the halo occupation distribution of CMASS galaxies, the radial density profile of the dark matter halos in which they reside and comparison with simulations, as well as limits on the stellar masses of these galaxies and their comparison to stellar population synthesis models. In this paper, we focus on the cosmological constraints on the matter density parameter,  $\Omega_m$  and the amplitude of density fluctuations quantified by  $\sigma_8$ .

This paper is organized as follows. In Section 2, we introduce the data products used to perform our analysis. We describe the measurements of the galaxy clustering and the galaxy-galaxy lensing signal in Section 3. In Section 4, we present the theoretical background for how these measurements can constrain cosmological parameters and the analytical halo occupation distribution model we use to interpret the data. The results of our main analysis and a variety of systematics tests are presented in Section 5. We conclude in Section 6 with a summary of our results and discuss the outlook for ongoing and future surveys.

We will assume a flat  $\Lambda$ CDM cosmology with  $\Omega_m = 0.27$  when converting redshifts to distances for performing the clustering and lensing measurements. Throughout this paper,  $\log$  denotes the 10-based logarithm of a quantity, the symbols  $h$  and  $h_{70}$  denote the Hubble constant,  $H_0$  normalized by  $100 \text{ km s}^{-1} \text{ Mpc}^{-1}$  and  $70 \text{ km s}^{-1} \text{ Mpc}^{-1}$ , respectively.

## 2. DATA

### 2.1. SDSS-III BOSS galaxies for clustering measurements

For this project, we use the sample of galaxies compiled in Data Release 11 (DR11) of the SDSS-III project. The SDSS-III is a spectroscopic investigation of galaxies and quasars selected from the imaging data obtained by the SDSS (York et al. 2000) I/II covering about  $11,000 \text{ deg}^2$  (Abazajian et al. 2009) using the dedicated 2.5-m SDSS Telescope (Gunn et al. 2006). The imaging employed a drift-scan mosaic CCD camera (Gunn et al. 1998) with five photometric bands ( $u, g, r, i$  and  $z$ ) (Fukugita et al. 1996; Smith et al. 2002; Doi et al. 2010). The SDSS-III (Eisenstein et al. 2011) BOSS project (Ahn et al. 2012; Dawson et al. 2013) obtained additional imaging data of about  $3,000 \text{ deg}^2$  (Aihara et al. 2011). The imaging data was processed by a series of pipelines (Lupton et al. 2001; Pier et al. 2003; Padmanabhan et al. 2008) and corrected for Galactic extinction (Schlegel et al. 1998) to obtain a reliable photometric catalog. This catalog was used as an input to select targets for spectroscopy (Dawson et al. 2013) for conducting the BOSS survey (Ahn et al. 2012) with the SDSS spectrographs (Smee et al. 2013). Targets are assigned to tiles of diameter  $3^\circ$  using an adaptive tiling algorithm designed to maximize the number of targets that can be successfully observed (Blanton et al. 2003). The resulting data were processed by an automated pipeline which performs spectral classification, redshift determination, and various parameter measurements, e.g., the stellar mass measurements from a number of different stellar population synthesis codes which utilize the photometry and redshifts of the individual galaxies (Bolton et al. 2012). In addition to the galaxies targeted by the BOSS project, we also use galaxies which pass the target selection but have already been observed as part of the SDSS-I/II project (legacy galaxies). These legacy galaxies are subsampled in each sector so that they obey the same completeness as that of the CMASS sample (Anderson et al. 2014).

To perform measurements of the clustering and lensing signals, we create various subsamples of the parent large scale structure catalog provided with DR11. To define the subsamples we use for the analysis, we make use of the stellar masses processed through the Portsmouth stellar population synthesis code (Maraston et al. 2013) with the assumptions of a passively evolving stellar population synthesis model and a Kroupa (2001) initial mass function. The top panel of Figure 1 shows the distribution of a random subsample of all galaxies in the large scale structure catalog in the stellar mass-redshift plane. The number density of this sample varies as a function of redshift and peaks at  $z \sim 0.55$ . The fiducial subsample we use in this paper, denoted as sample A, consists of all galaxies between  $z \in [0.47, 0.59]$  and with  $\log M_*/h_{70}^{-2} M_\odot \in [11.1, 12.0]$ . This selection results in a sample with an approximately uniform number density with redshift compared to the parent sample. The number density of this fiducial sample is  $\sim 3 \times 10^{-4} h^3 \text{ Mpc}^{-3}$ . The total number

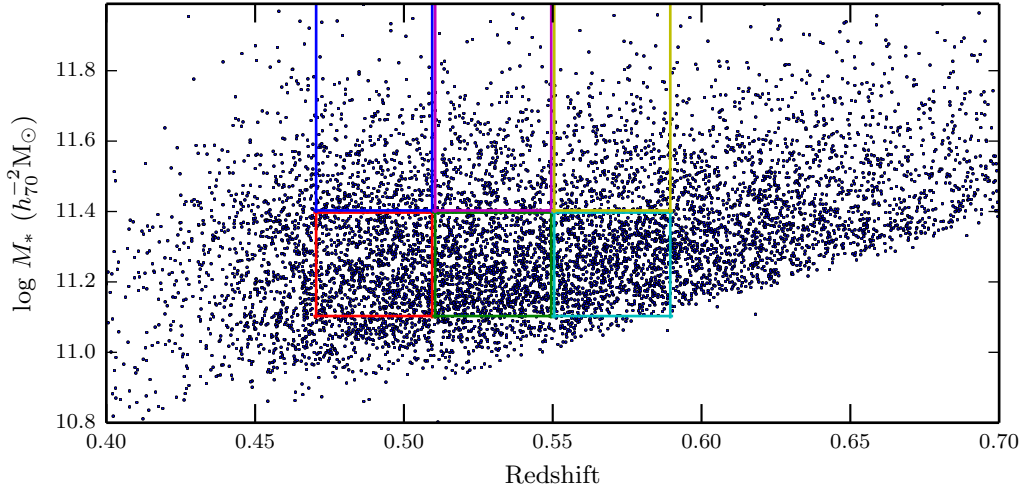


**Figure 1.** The CMASS galaxy sample in the redshift–stellar mass plane. The fiducial sample in this study corresponds to the redshift range  $z \in [0.47, 0.59]$  and stellar mass range  $\log M_* \in [11.1, 12.0]$ . To investigate the redshift and stellar mass dependence of the clustering we further subdivide this sample into six bins indicated by different colour boxes in this figure. In addition, we will investigate the robustness of the cosmological constraints with samples that span the same redshift range as our fiducial sample but progressively restricting the samples to more massive galaxies,  $\log M_* \in [11.3, 12.0]$  and  $\log M_* \in [11.4, 12.0]$ . To avoid crowding we show only 1 percent of the total sample in this figure.

of galaxies in this sample is 378 807 (400 916)<sup>1</sup> and constitutes about 50 percent of the parent sample used for the measurements of the baryon acoustic oscillations. We will also consider the subsamples of galaxies (as shown by the different color boxes in Figure 1) to test how the clustering of galaxies varies as a function of redshift and stellar mass. Finally, in order to test the effects of incompleteness at the low stellar mass end in our fiducial subsample on our cosmological constraints, we additionally consider two different subsamples of galaxies which lie in the same redshift range but where the stellar mass selection is  $\log M_*/h_{70}^{-2} M_\odot \in [11.30, 12.0]$  and  $\log M_*/h_{70}^{-2} M_\odot \in [11.40, 12.0]$ , respectively. These subsamples will be denoted as *B* and *C*, respectively. The numbers of galaxies in these subsamples are 196578 and 116682 (these numbers include fiber collided and redshift failure galaxies), while the number densities of the galaxies are  $1.5 \times 10^{-4}$  and  $0.8 \times 10^{-4} h^3 \text{Mpc}^{-3}$ , respectively. The number density of galaxies is approximately constant in the redshift range we use.

We must account for a number of subtle selection effects in order to obtain a precise measurement of clustering (Ross et al. 2012). The spectroscopic target sample is obtained from the SDSS imaging observations after the application of a variety of colour and photometric selection cuts (Dawson et al. 2013). However, due to the limited number of fibers available, not all galaxies from this target sample can be allocated a fiber while performing spectroscopic observations to determine their redshifts. This could also happen if two targets are within  $62''$  of each other and hence they cannot be simultaneously observed due to the finite size of fibers. If such fiber-collided galaxies lie in a region of the sky which is visited multiple times (due to overlaps in the target tiling) then they may have redshift measurements. There are also instances where a galaxy is assigned to a fiber, but its redshift could not be obtained. Finally, there are also instances where it is difficult to perform star-galaxy separation, especially in fields

with a high number density of stars. These effects have been quantified in the parent DR11 catalog of CMASS galaxies by assigning a weight to each galaxy such that

$$w_l = w_* (w_{\text{noz}} + w_{\text{cp}} - 1), \quad (1)$$

where  $w_{\text{noz}}$  is the weight assigned to a galaxy if it is the nearest neighbour (in the plane of the sky) of a redshift failure galaxy,  $w_{\text{cp}}$  is similarly assigned to account for the nearest neighbours of fiber collided galaxies<sup>2</sup>, and  $w_*$  accounts for the systematic relationship between density of stars and density of BOSS target galaxies (for details, see Anderson et al. 2014). The BOSS parent catalog contains an additional weight,  $w_{\text{FKP}}$ , for each galaxy which depends upon the number density of galaxies in the sample at its redshift (Feldman et al. 1994). This weight is important for the parent galaxy catalog which has a much larger variation in the number density of galaxies than the variation in  $\bar{n}(z)$  for the subsamples of galaxies we use. Therefore, in our analysis, we do not include this weight.

The weights  $w_{\text{noz}}$  and  $w_{\text{cp}}$  can only be used if the entire sample of galaxies within a given redshift range is used to measure the clustering signal. In particular, for the subsamples of galaxies selected by stellar mass (or luminosity), it is unclear whether the fiber-collided or redshift-failure galaxy will be part of our subsample if it is assigned the same redshift as its nearest neighbour, as it may or may not satisfy the stellar mass cut we have imposed. If we were to use the weights  $w_{\text{noz}}$  and  $w_{\text{cp}}$  as provided, then we would spuriously include the weights of some galaxies which should not be in the subsample. We will also miss some fiber-collided or redshift-failure galaxies which should have been part of our subsample because their nearest neighbours failed to make it to our subsample due to stellar mass cuts. In addition there is a possibility that the small scale clustering will be affected by using the weights, as all pairs of galaxies involving a fiber-collided or redshift-failure galaxy are assigned line-of-sight separations equal to zero.

<sup>1</sup> The number in parentheses includes galaxies with redshift failures and those that could not be allocated fibers to measure their redshifts (fiber collided galaxies) as described in the next paragraph.

<sup>2</sup> Both  $w_{\text{noz}}$  and  $w_{\text{cp}}$  are equal to unity by default for all galaxies. Their values are incremented for the nearest neighbours of every redshift failure or fiber collided galaxy.

Given these issues, we refrain from using the weights  $w_{\text{noz}}$  and  $w_{\text{cp}}$  in our analysis. Instead, we have obtained the stellar masses using the measured photometry of the fiber-collided and the redshift-failure galaxies with the redshift of its nearest neighbour. Each of these galaxies are assigned the same  $w_*$  as their nearest neighbours. We have verified that the stellar mass-redshift distribution of such galaxies is similar to that of the sample of galaxies which have well measured redshifts (catastrophic failures in the nearest neighbour redshift assumption will result in both an incorrect redshift and stellar mass). We then decide whether to include these galaxies in our subsample based on whether these galaxies pass the stellar mass cuts we impose.

## 2.2. CFHTLenS galaxies for lensing measurements

For the measurements of the galaxy-galaxy lensing signal around the subsamples of CMASS galaxies, we must measure the tangential distortion of background galaxies. For this purpose, we rely on the deeper and better quality imaging data from the Canada France Hawaii Telescope Legacy survey (CFHTLS). This information allows us to measure the tangential distortion of background galaxies around our sample of CMASS galaxies. In particular we make use of the photometric reduction and image shape determinations in the publicly available CFHTLenS catalog<sup>3</sup>. The quantities needed for each galaxy, namely its shear estimate, calibration factors, weight, and photometric redshift are provided in the catalog (Heymans et al. 2012; Erben et al. 2013; Miller et al. 2013; Hildebrandt et al. 2012). Unfortunately, the overlap between the CFHTLS and the DR11 BOSS fields is limited to an area of only  $\approx 100 \text{ deg}^2$ . The number of CMASS galaxies that lie within the CFHTLS footprint is 5084 for our fiducial subsample A, 2549 from subsample B and 1577 for subsample C.

We compare the probability distribution of the stellar mass,  $P(\log M_*)$ , and that of the redshifts,  $P(z)$ , for the subsample of galaxies we use for our cosmological analyses in the CFHT region to those in the entire CMASS region in the panels of Figure 2. Although the stellar mass distributions in the CFHT region is not particularly special, the redshift distributions shows some noticeable differences, presumably due to the structures in the CFHT field. We assessed the systematics of the differences in the redshift distribution by including a weight  $w_{\text{sys}}(z) = p^{\text{CMASS}}(z)/p^{\text{CFHT}}(z)$  when calculating the weak lensing signal. The differences in the lensing signal when including this weight are of the order 2 percent, much smaller than our errorbars on the lensing signal. We therefore conclude that this weight is not needed for the analysis, and that the sample of CMASS galaxies in the CFHT fields is sufficiently close to a fair sample for our purposes.

## 3. MEASUREMENTS

To measure the clustering and lensing signals around BOSS galaxies, we assume a fiducial flat  $\Lambda$ CDM cosmological model with  $\Omega_m = 0.27$  to convert the differences in the angular positions and redshifts of galaxies to projected and line-of-sight separations between galaxies. While inferring the cosmological parameters using these measurements, we will account for the choice of the fiducial cosmology assumed for the measurements as described in Section 4.2 (see also More 2013).

<sup>3</sup> <http://www.cfhtlens.org/astronomers/data-store>

### 3.1. Clustering of BOSS galaxies

The clustering of galaxies can be quantified using the two-point correlation function. The two-point correlation function,  $\xi(r)$ , depends only upon the true three-dimensional distance between galaxies,  $r$ , if the Universe is isotropic. However, the isotropy is broken due to the modulation in the distances of galaxies along line-of-sight ( $\pi$ ) caused by the peculiar motions of galaxies compared to the distances along the plane of the sky ( $r_p$ ). The resultant correlation function displays a characteristic anisotropic pattern which elongates (flattens) the iso-correlation contours in the  $(r_p, \pi)$  plane on small (large) projected scales. The impact of such effects can be minimized by focusing on the projected two-point correlation function obtained by integrating the correlation function  $\xi(r_p, \pi)$  along the line-of-sight,

$$w_p(r_p) = 2 \int_0^{\pi_{\text{max}}} \xi(r_p, \pi) d\pi. \quad (2)$$

Unless stated otherwise, we will use  $\pi_{\text{max}} = 100 h^{-1} \text{Mpc}$ , and employ the same finite line-of-sight integration limit while analytically modelling the observations.

We use the estimator proposed by Landy & Szalay (1993),

$$\xi(r_p, \pi) = \frac{DD - 2DR + RR}{RR} \quad (3)$$

to obtain the two-point correlation function  $\xi(r_p, \pi)$ . Here,  $DD$ ,  $RR$  and  $DR$  represent the number of appropriately weighted pairs of galaxies with a given separation  $(r_p, \pi)$ , where both galaxies lie either in the galaxy catalog or the random catalog or one in each of the catalogs, respectively.

We use random catalogues with the same angular and redshift selection as our galaxy sample. These random catalogs consist of about 50 times more points than the number of galaxies in each of our samples. We assign each random point a weight of  $N_{\text{gal}}/N_{\text{ran}}$  to account for this difference. In practice, we use the random catalogs provided with SDSS DR11 (Anderson et al. 2014), appropriately downsampled to account for the difference in the redshift distribution due to our sample selection.

In Figure 3, we present the clustering signals of galaxy subsamples enclosed in the six color boxes in Figure 1. Each panel shows the dependence of the clustering signal on stellar mass selection at fixed redshift<sup>4</sup>. This figure demonstrates that the clustering signal varies with stellar mass at fixed redshift. Given that the stellar mass threshold of the full sample of CMASS galaxies varies with redshift, the stellar mass dependence of the clustering signal implies the necessity of a proper redshift dependent modelling of the clustering if the entire galaxy sample is used. In this paper, instead, we use the subsamples that are defined by constant stellar mass thresholds in a given redshift range (see Figure 1). In Figure 4, we show that the clustering signals of the stellar mass limited subsamples do not vary substantially with redshift. Although not a formal justification, this result supports our assumption of a single effective redshift for modelling our measurements.

Utilizing galaxies from a single redshift bin  $z \in [0.47, 0.59]$ , we plot the projected clustering signals for the three subsamples of CMASS galaxies in the left-hand panel of Figure 5,

<sup>4</sup> We use a line-of-sight integration length  $\pi_{\text{max}} = 60 h^{-1} \text{Mpc}$  for projecting the redshift space correlation function for these tests only given the limited redshift range of the data. Everywhere else in the paper we use  $\pi_{\text{max}} = 100 h^{-1} \text{Mpc}$ .

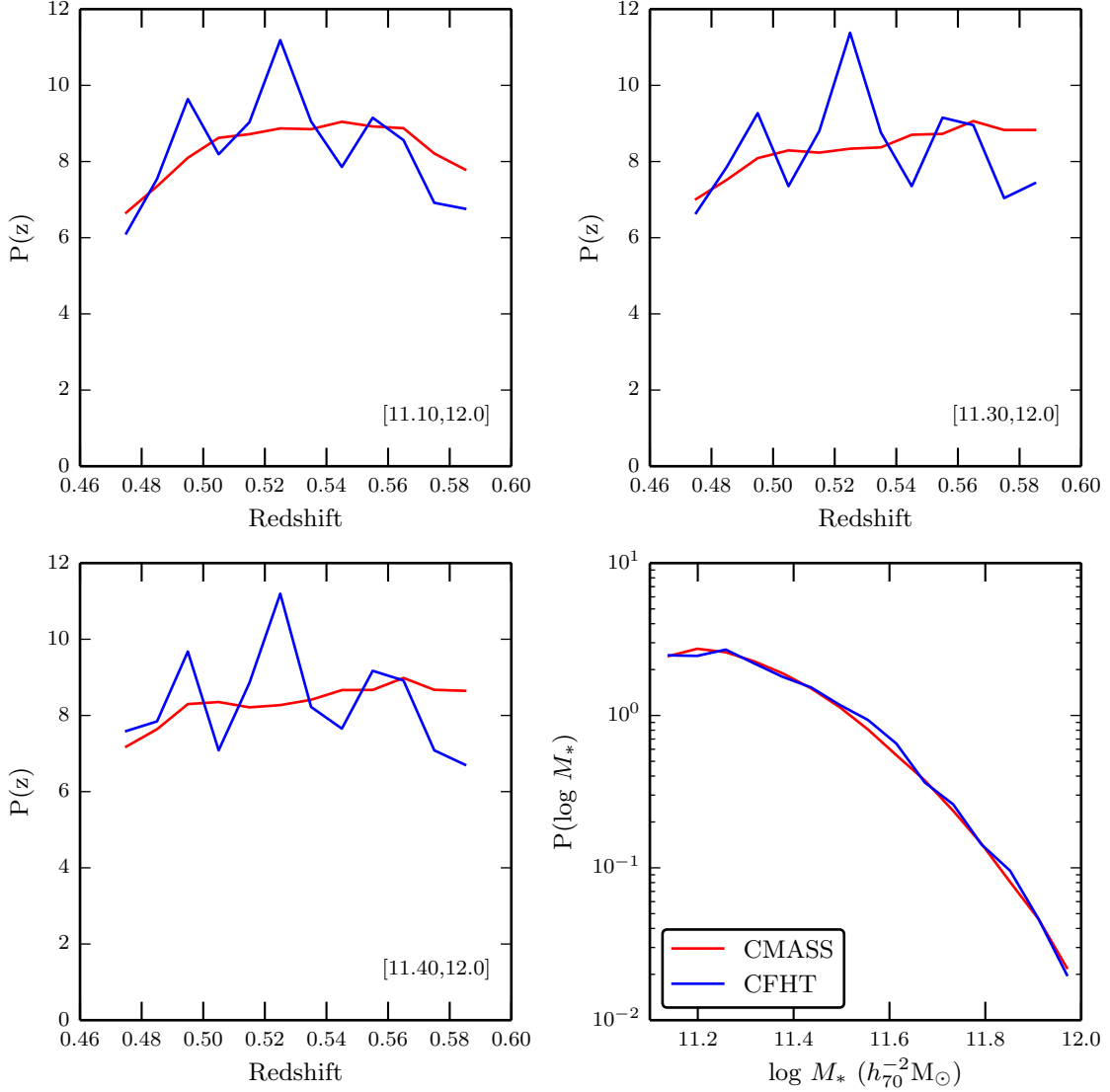


**Figure 2.** The comparison of the redshift distributions of galaxies in the CFHT fields (blue solid line) and those in the CMASS fields (red solid line) for the three stellar mass subsamples we use for our cosmological analysis are shown in the top left, top right and bottom left panels. The bottom right panel shows a similar comparison but for the stellar mass distribution of galaxies. The stellar mass distribution of the CFHT subsample appears fairly representative of that of the entire CMASS population. The redshift distribution shows noisy deviations due to structures in the CFHT regions. We will explore how these deviations could affect our cosmological parameter estimates in Section 5.

which we will use for our cosmological analysis. The errorbars are obtained using the jackknife technique, where we utilized 192 jackknife regions on the sky covering the entire survey footprint. The covariance matrix of the projected clustering measurement in each of our subsamples (normalized to have a value of unity on the diagonals) are shown in each of the panels of Figure 6. There is a significant covariance between the errorbars of the measurements on large scales, and we include this covariance while modelling the signal. The total signal-to-noise ratio of the clustering in our fiducial subsample is 55.6, properly accounting for the covariance. It decreases to total signal-to-noise ratios of 48.3 and 39.7 for the subsamples B and C, respectively.

### 3.2. Lensing around BOSS galaxies

The shapes of background galaxies are affected by the intervening matter between the galaxies and Earth. Since galaxies reside in dark matter halos, the ellipticities of background

galaxies behind foreground lens galaxies (for example, those in our CMASS sample) are expected to be aligned preferentially in a tangential direction with respect to the lensing galaxy. As described in Section 2, we make use of the CFHTLenS catalog of background galaxies to detect and measure this preferential tangential alignment of the ellipticities,  $\langle e_t \rangle$ . The average tangential ellipticity in annuli around the CMASS galaxies in the weak lensing regime is equal to the tangential shear  $\langle \gamma_t \rangle$  and is related to the projected matter distribution  $\Sigma(r_p)$  via

$$\langle e_t \rangle = \langle \gamma_t \rangle = \frac{\Delta \Sigma(r_p)}{\Sigma_{\text{crit}}}. \quad (4)$$

Here  $\Delta \Sigma(r_p)$  is given by

$$\Delta \Sigma(r_p) = \bar{\Sigma}(r_p) - \langle \Sigma(< r_p) \rangle \quad (5)$$

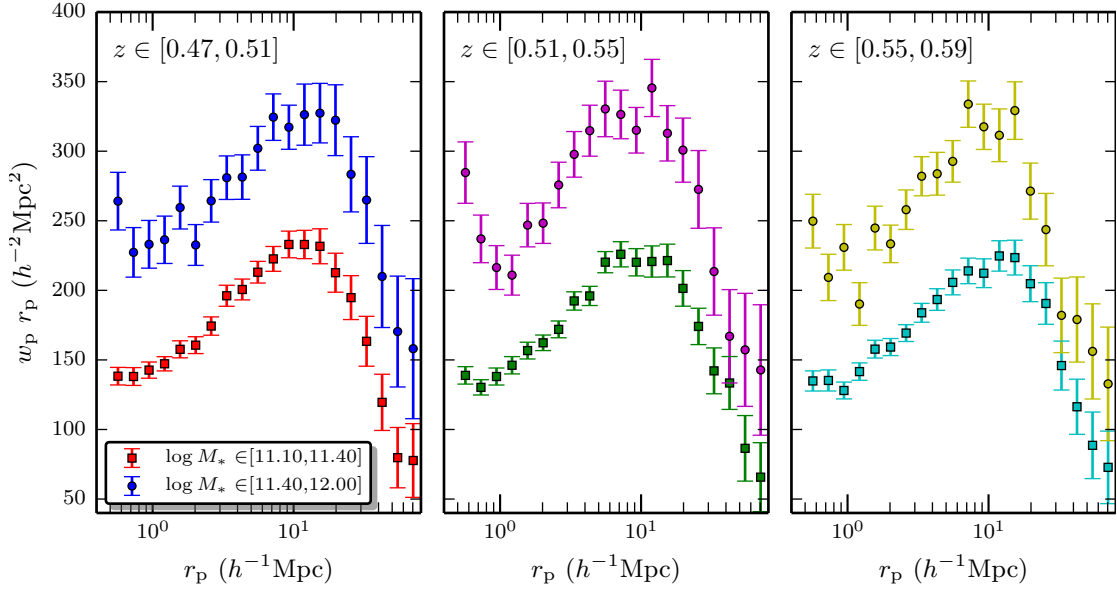


**Figure 3.** The stellar mass dependence of the projected clustering signal at fixed redshift is displayed in each of the panels for three different redshift bins. Data points with errorbars show the clustering measurements of the different subsamples shown in Figure 1. Squares with errorbars correspond to the stellar mass bin  $\log M_*/h_{70}^{-2}M_\odot \in [11.10, 11.40]$  while circles with errorbars correspond to the stellar mass bin  $\log M_*/h_{70}^{-2}M_\odot \in [11.40, 12.00]$ . The line-of-sight integration length used to project the redshift space correlation function is  $60 h^{-1}\text{Mpc}$ . At fixed redshift, the clustering amplitude increases strongly with the stellar mass of galaxies.

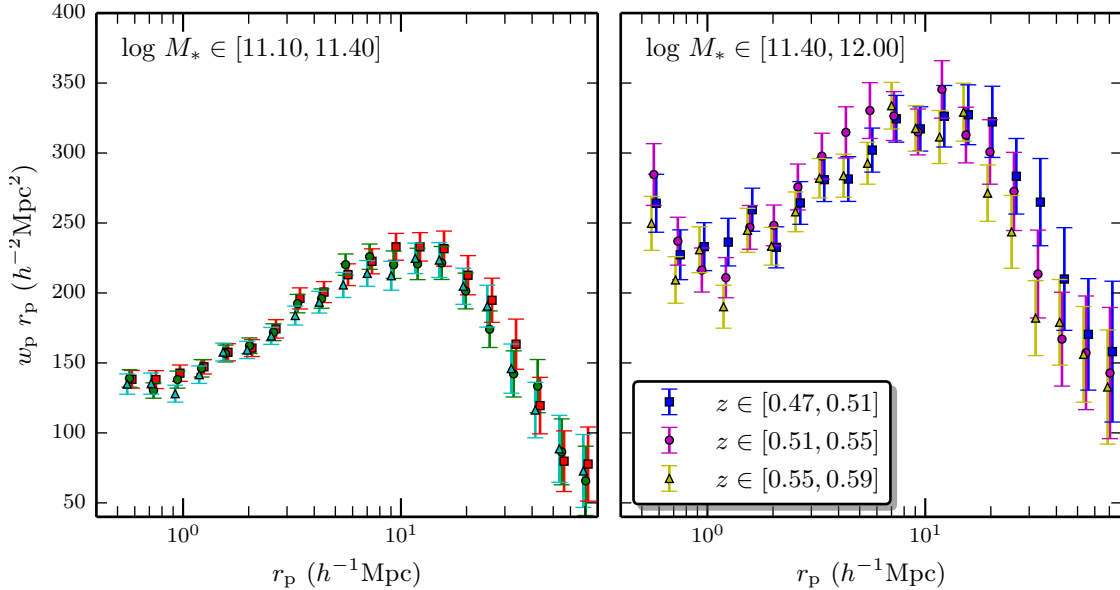


**Figure 4.** The left and the right panels display the redshift dependence of the clustering signal at fixed stellar mass for two different stellar mass bins. Data points with errorbars show the clustering measurements of the different subsamples shown in Figure 1. In each panel, squares with errorbars, circles with errorbars, and triangles with errorbars are used to denote the measurement of clustering in the redshift bins  $[0.47, 0.51]$ ,  $[0.51, 0.55]$  and  $[0.55, 0.59]$ , respectively. The line-of-sight integration length used to project the redshift space correlation function is  $60 h^{-1}\text{Mpc}$ . We have shifted the lowest (highest) redshift bin points to the right (left) by a small amount for clarity. For fixed stellar mass bins, the clustering amplitude varies very weakly with redshift.

where  $\bar{\Sigma}(r_p)$  is the average surface mass density in the annuli and  $\langle \Sigma(< r_p) \rangle$  is the average density within a circle of radius  $r_p$ . The quantity  $\Sigma_{\text{crit}}$  is the critical density which for the assumed cosmology and the measured redshifts of source and lens galaxies is given by

$$\Sigma_{\text{crit}}(z_l, z_s) = \frac{c^2}{4\pi G} \frac{d_A(z_s)}{d_A(z_l)d_A(z_l, z_s)(1+z_l)^2}, \quad (6)$$

where  $d_A(z_s)$  and  $d_A(z_l)$  are angular diameter distances of source and lens galaxy, respectively, and  $d_A(z_l, z_s)$  is angu-

lar diameter distance between the lens and source galaxy. The factor of  $(1+z_l)^2$  in the denominator is due to our choice of comoving coordinates.

Since the lens and the source galaxies do not lie at the same redshift, we use a minimum variance estimator to measure  $\Delta\Sigma$  around our subsamples of CMASS galaxies. More details of the lensing measurements and the covariance for our fiducial CMASS subsample A are described in detail in our companion paper (Miyatake et al. 2013). The total signal-to-noise ratios of the lensing measurements for this subsample is 26.1, even given the small overlapping area,  $\sim 100 \text{ deg}^2$ . We ap-

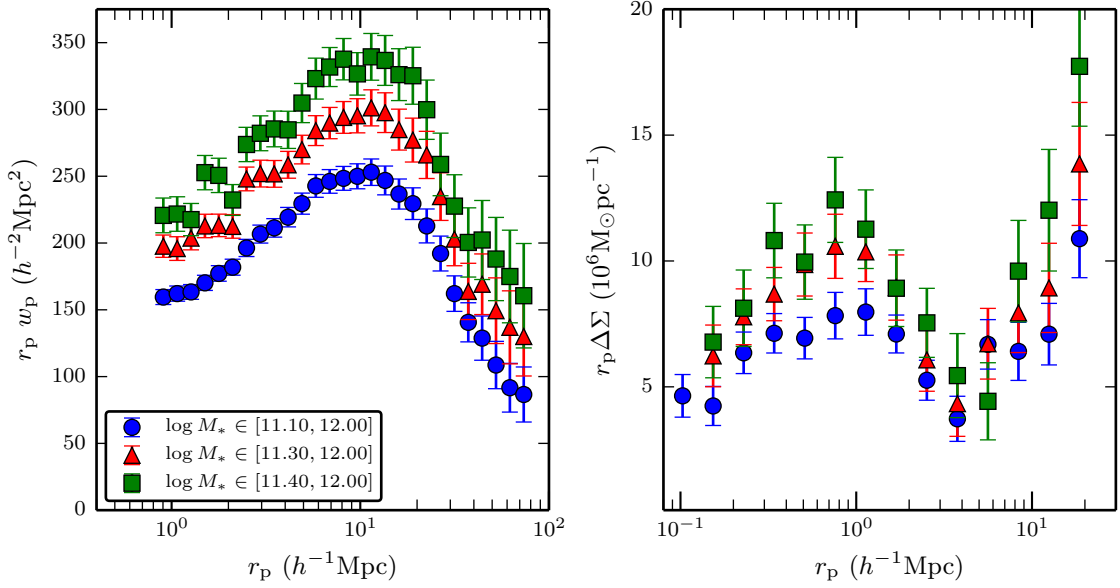


**Figure 5.** The clustering (left) and the lensing (right) signal measurements for samples in the redshift range  $z \in [0.47, 0.59]$  but with stellar mass threshold cuts  $\log M_* > 11.10, 11.30$  and  $11.40$  are shown using blue circles with errors, red triangles with errors and green squares with errors, respectively. The line of sight integration length used to project the redshift-space correlation function is  $100 h^{-1} \text{Mpc}$  for all the three subsamples. These measurements will be used to constrain the halo occupation distribution parameters of galaxies as well as the cosmological parameters.

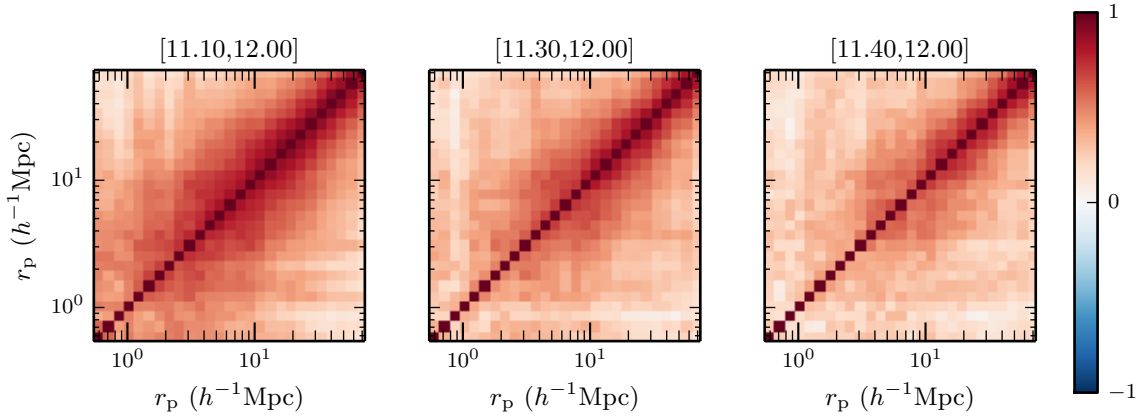


**Figure 6.** The correlation matrix of the clustering measurements for the samples used for cosmological parameter analyses in this study obtained using 192 jack-knife samples. The covariance will be used while calculating the likelihood of the clustering measurements given the parameters. The lensing measurements also has its corresponding covariance (see Paper I).

plied the same analysis method for subsamples B and C and obtained measurements with signal-to-noise ratios of 24.5 and 21.3, respectively. The lensing signals for all the three subsamples are shown as points with errorbars in the right hand panel of Figure 5. We use these measurements of the galaxy-galaxy lensing signal together with the galaxy-galaxy clustering signal in order to constrain our model parameters. We did not include the innermost radial bin for subsample C, because this bin shows a relatively large boost factor for the correction and does not appear reliable (for details of the boost factor, see Miyatake et al. 2013).

#### 4. THEORY

Structure formation in the concordance  $\Lambda \text{CDM}$  cosmological model occurs as a result of the gravitational collapse of initial density fluctuations into extended halos of dark matter. The abundance of halos in different cosmological models has a universal form when expressed as a function of peak

height,  $\nu = \delta_c / \sigma$ , where  $\delta_c$  is the critical threshold for collapse,  $\sigma(M, z)$  is the variance of density fluctuations smoothed on spatial scales corresponding to the comoving radius from which the halo mass  $M$  assembled (e.g., Mo & White 1996b; Sheth & Tormen 1999). These halos form preferentially at the peaks of the matter density field and hence are biased with respect to the matter distribution. The halo bias can also be expressed as a function of the peak height. Galaxies share the bias of the halos in which they reside. The overall clustering amplitude at sufficiently large separation is determined by the products of this bias ( $b$ ), the amplitude of the linear matter fluctuations ( $\sigma_8$ ) and the growth rate of fluctuations at a given redshift ( $D(z)$ );  $w_p(r_p) \propto [b\sigma_8 D(z)]^2$ .

Figure 7 displays the dependence of the clustering amplitude of halos as a function of their mass on cosmological parameters. In the left hand panel,  $\sigma_8$  is fixed while the matter density,  $\Omega_m$ , is varied for flat  $\Lambda \text{CDM}$  cosmological models. In the right hand panel,  $\Omega_m$  is fixed while  $\sigma_8$  is varied. In-

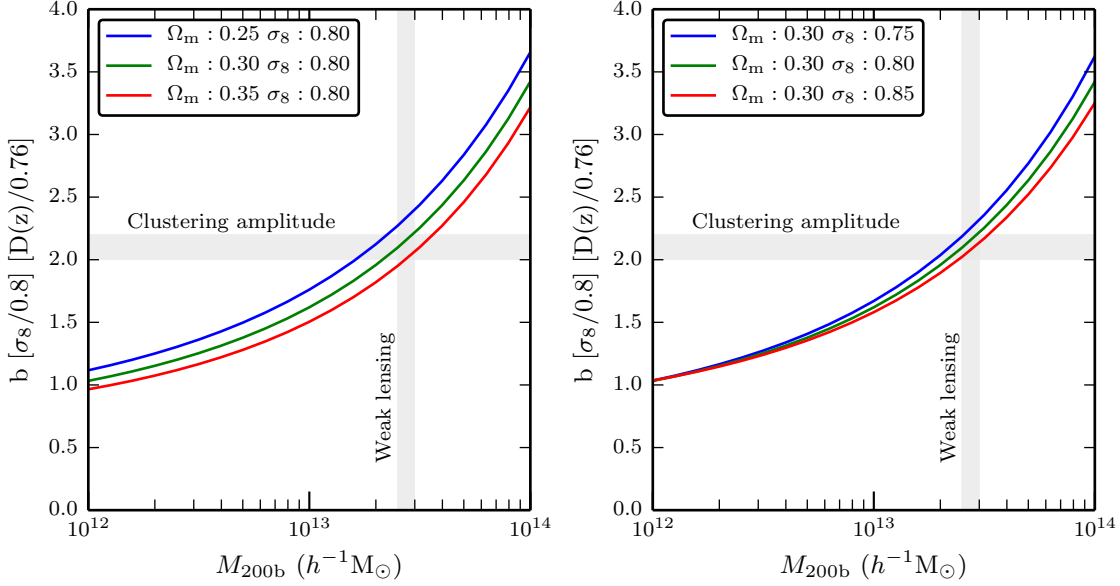


**Figure 7.** Theoretical predictions of the amplitude of the galaxy clustering signal on large scales as a function of the halo mass of these galaxies in different cosmological models. The left hand panel shows how the clustering amplitude varies when  $\Omega_m$  is increased, while the right hand panel shows the corresponding change when  $\sigma_8$  is increased. Measurements of the clustering of galaxies and the galaxy-galaxy lensing signal determine the ordinate and the abscissa, respectively, thus allowing constraints on these cosmological parameters.

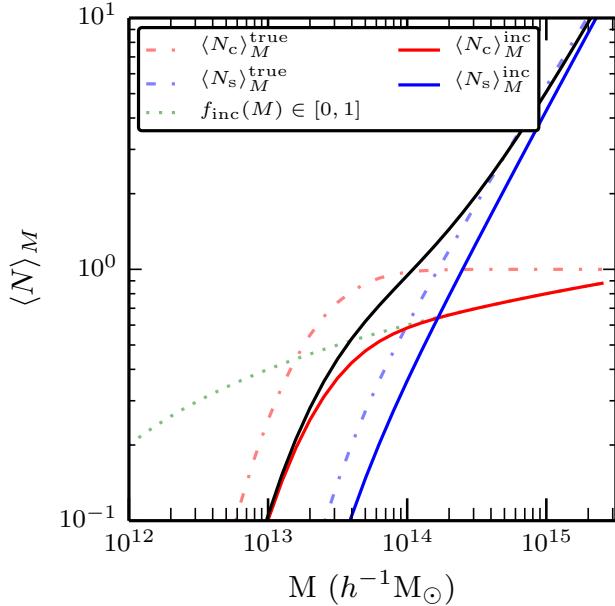


**Figure 8.** An illustration of the halo occupation distribution model we use in the analysis of this paper. The red and blue dot-dashed lines show the central and satellite components of the HOD appropriate for a true stellar mass threshold sample. The green dotted line shows the log-linear functional form we assume for parameterizing the incompleteness in our subsample. The solid red, blue and black lines show the HOD of centrals, satellites and all galaxies after accounting for the incompleteness. In total our HOD model is parametrized by 7 parameters.

ing both  $\Omega_m$  and  $\sigma_8$  results in a decrease of the clustering amplitude at fixed halo mass. The measurement of the clustering amplitude of galaxies fixes the clustering amplitude of halos in which they reside. However, one can obtain similar clustering amplitudes in different cosmological models by changing the halos in which galaxies reside. This behavior is

the classical degeneracy between halo occupation distribution parameters and the cosmological parameters; one can obtain the same clustering amplitude for galaxies by having them reside in larger mass halos in cosmologies with larger  $\Omega_m$  or  $\sigma_8$ . The weak lensing signal on small scales breaks this degeneracy by direct inference of the mass of the halos, thus allowing a determination of cosmological parameters. Given the errors in determination of the clustering amplitude and the halo mass, we expect degeneracy in the determination of  $\Omega_m$  and  $\sigma_8$  such that increasing the value of one can be compensated by decreasing the value of the other.

The above qualitative picture is valid if galaxies occupy a narrow range of halo masses. In reality, in our stellar mass threshold samples, galaxies span a range in halo masses. In addition, although most galaxies are central galaxies in their halos, some of those in our subsample are satellite galaxies. The average clustering amplitude,  $A_{\text{gal}}$ , is related to the bias of halos through an integral over the halo occupation distribution of the galaxies in our subsample,

$$\begin{aligned} \langle A \rangle_{\text{gal}} &= \sigma_8 D(z) b_{\text{eff}} \\ &= \sigma_8 D(z) \frac{\int dM \langle N \rangle_M b(M, z) n(M, z)}{\int dM \langle N \rangle_M n(M, z)}, \end{aligned} \quad (7)$$

where the ratio of the integrals is the effective bias ( $b_{\text{eff}}$ ) of the galaxy sample. Similarly, the average mass of halos as determined from the weak lensing signal needs to appropriately account for the halo occupation distribution of the galaxies.

#### 4.1. Analytical HOD model

We use a halo occupation distribution model (hereafter HOD; Jing et al. 1998; Peacock & Smith 2000; Seljak 2000a; Scoccimarro et al. 2001; Zheng et al. 2005; Leauthaud et al. 2012; van den Bosch et al. 2013; Cacciato et al. 2013a,b), to predict the abundance, the clustering and the lensing signal of CMASS galaxies. We adopt an HOD model with an explicit



split of the halo occupation into central and satellite galaxies,

$$\langle N \rangle_M = \langle N_c \rangle_M + \langle N_s \rangle_M \quad (8)$$

The mean halo occupation distribution for central galaxies is given by

$$\langle N_c \rangle_M = f_{\text{inc}}(M) \frac{1}{2} \left[ 1 + \text{erf} \left( \frac{\log M - \log M_{\text{cut}}}{\sigma_{\log M}} \right) \right], \quad (9)$$

and that for satellite galaxies is given by

$$\langle N_s \rangle_M = \langle N_c \rangle_M \left[ \frac{M - \kappa M_{\text{cut}}}{M_1} \right]^\alpha \quad (10)$$

when  $M > \kappa M_{\text{cut}}$  and zero otherwise (see e.g., Zheng et al. 2005; White et al. 2011). The function  $f_{\text{inc}}(M)$  accounts for potential incompleteness in the selection of CMASS galaxies at the low stellar mass end (see e.g., More et al. 2011; Reddick et al. 2013; Miyatake et al. 2013) when compared to a true stellar mass threshold sample. We assume a log-linear functional form for the incompleteness function such that

$$f_{\text{inc}}(M) = \max[0, \min[1, 1 + \alpha_{\text{inc}}(\log M - \log M_{\text{inc}})]] \quad (11)$$

This model explicitly assumes that the CMASS selection selects a random fraction of the stellar mass threshold galaxies, given by  $f_{\text{inc}}$ , from host halos at every mass scale, equivalently, it assumes that with the CMASS color and magnitude cuts, the selection probability for galaxies at a given stellar mass do not depend on the environment or other properties.

We follow the analytical framework developed in van den Bosch et al. (2013) (with a minor extension to account for the miscentering of central galaxies with respect to their halo centers), to predict the galaxy-galaxy clustering and the galaxy-galaxy lensing signal, using the halo occupation distribution described above. We briefly present the key expressions below for completeness.

The galaxy-galaxy power spectrum,  $P_{\text{gg}}(k, z)$ , is the Fourier transform of the galaxy correlation function,  $\xi(r, z)$  and can be expressed as a sum of the following one- and two-halo terms,

$$P_{\text{gg}}(k, z) = 2 P_{\text{cs}}^{\text{1h}}(k, z) + P_{\text{ss}}^{\text{1h}}(k, z) + P_{\text{cc}}^{\text{2h}}(k, z) + 2 P_{\text{cs}}^{\text{2h}}(k, z) + P_{\text{ss}}^{\text{2h}}(k, z). \quad (12)$$

Here the subscripts ‘c’ and ‘s’ stand for central and satellite galaxy, respectively. Each of these terms can be expressed in the following compact form

$$P_{\text{xy}}^{\text{1h}}(k, z) = \int dM \mathcal{H}_x(k, M, z) \mathcal{H}_y(k, M, z) n(M, z), \quad (13)$$

$$P_{\text{xy}}^{\text{2h}}(k, z) = \int dM_1 \mathcal{H}_x(k, M_1, z) n(M_1, z) \times \int dM_2 \mathcal{H}_y(k, M_2, z) n(M_2, z) Q(k|M_1, M_2, z), \quad (14)$$

where ‘x’ and ‘y’ are either ‘c’ (for central) or ‘s’ (for satellite),  $n(M, z)$  describes the halo mass function at redshift  $z$ ,  $Q(k|M_1, M_2, z)$  describes the power-spectrum of haloes of masses  $M_1$  and  $M_2$  and accounts for the radial dependence of bias, non-linearities in the matter power spectrum and halo exclusion, ingredients that can be calibrated by numerical simulations (see, e.g., van den Bosch et al. 2013). Furthermore,

we have defined

$$\mathcal{H}_c(k, M, z) = \frac{\langle N_c \rangle_M}{\bar{n}_g(z)} \left( 1 - p_{\text{off}} + p_{\text{off}} \exp \left[ -\frac{1}{2} k^2 (r_s \mathcal{R}_{\text{off}})^2 \right] \right), \quad (15)$$

and

$$\mathcal{H}_s(k, M, z) = \frac{\langle N_s \rangle_M}{\bar{n}_g(z)} \tilde{u}_s(k|M, z). \quad (16)$$

Here, we have assumed that there is a fraction  $p_{\text{off}}$  of central galaxies that are offset from the center of their halos (see e.g., Skibba et al. 2011) and that the normalized radial profile of the off-centered galaxies, with respect to the true halo center, is a Gaussian with width relative to the scale radius,  $r_s$ , of the halo in which they reside,

$$u_{\text{off}}(r|M) = \frac{1}{(2\pi)^{3/2} (r_s \mathcal{R}_{\text{off}})^3} \exp \left[ -\frac{1}{2} \left( \frac{r}{r_s \mathcal{R}_{\text{off}}} \right)^2 \right]. \quad (17)$$

The Fourier transform of  $u_{\text{off}}(r|M)$  is  $\exp[-k^2 (r_s \mathcal{R}_{\text{off}})^2 / 2]$ , and the quantity  $\tilde{u}_s(k|M)$  in  $\mathcal{H}_s(k, M, z)$  is the Fourier transform of an Navarro-Frenk-White (Navarro et al. 1996, hereafter NFW) profile for a halo of mass  $M$  (see also Hikage et al. 2013, for a similar model). We also assume that the normalized number density profile of satellite galaxies follows the NFW profile<sup>5</sup>. The number density of galaxies,  $\bar{n}_g(z)$ , is given by

$$\bar{n}_g(z) = \int \langle N \rangle_M n(M, z) dM \quad (18)$$

We will assume a  $\sim 20$  percent fractional error on the abundances, since our stellar mass cuts yield a roughly constant abundance with redshift, with  $\sim 20$  percent level fluctuations. In the presence of parameters to model the incompleteness we do not expect the abundances to influence the cosmological constraints in a significant manner.

The real-space correlation function,  $\xi_{\text{gg}}(r, z)$ , can be obtained by an inverse Fourier transform of the galaxy-galaxy power spectrum. We use a modified version of the large scale redshift space distortion model presented by Kaiser (1987) to predict  $\xi_{\text{gg}}^c(r_p, \pi, z)$  from  $\xi_{\text{gg}}(r, z)$  (see van den Bosch et al. 2013, for details), and use Equation (2) to calculate the projected correlation function. This modified model accounts for residual redshift space distortions on large scales due to finite value of  $\pi_{\text{max}}$  (see e.g., Norberg et al. 2009; Baldauf et al. 2010; More 2011; van den Bosch et al. 2013). The upper limit for the line-of-sight integration we adopt is  $\pi_{\text{max}} = 100 h^{-1} \text{Mpc}$ , thus mimicking the integration limit adopted in the measurements.

The galaxy-galaxy lensing signal is a probe of the excess surface density, which is given by Equation 5. The surface density  $\Sigma(r_p, z)$  can be obtained by projecting the galaxy-matter correlation function,  $\xi_{\text{gm}}(r, z)$ , using

$$\Sigma(r_p, z) = \int_R^\infty \bar{\rho} [1 + \xi_{\text{gm}}(r, z)] \frac{2 r dr}{\sqrt{r^2 - r_p^2}}. \quad (19)$$

In order to predict the galaxy-matter cross power spectrum,

<sup>5</sup> We have examined models which allow the satellite galaxies to have a concentration which is different from that of the dark matter distribution. The clustering signal on small scales is sensitive to this parameter. We model the clustering signal on scales larger than  $r_p > 0.85 h^{-1} \text{Mpc}$  where the impact of this parameter is minimal. We have verified that the cosmological constraints are robust to the inclusion or exclusion of such a parameter.

we adopt the HOD model framework. The cross power spectrum is given by the sum of the following one- and two-halo terms

$$P_{\text{gm}}(k, z) = P_{\text{cm}}^{\text{1h}}(k, z) + P_{\text{sm}}^{\text{1h}}(k, z) + P_{\text{cm}}^{\text{2h}}(k, z) + P_{\text{sm}}^{\text{2h}}(k, z). \quad (20)$$

Each of the above terms can be calculated using Eqs. (13)-(14), where ‘x’ is ‘m’ (for matter) and ‘y’ is either ‘c’ (for central) or ‘s’ (for satellite). For the matter component, we define

$$\mathcal{H}_m(k, M, z) = \frac{M}{\bar{\rho}_m(z)} \tilde{u}_h(k|M, z), \quad (21)$$

where  $\tilde{u}_h(k|M, z)$  is the Fourier transform of the normalized density distribution of matter within a halo of mass  $M$ , and  $\bar{\rho}_m(z)$  denotes the average comoving density of the Universe at redshift  $z$ . The galaxy-matter correlation function can be obtained by an inverse Fourier transform of the galaxy-matter power spectrum.

The lensing signal is sensitive to the total matter content of galaxies including both the dark matter and the baryonic components. Therefore, we will also consider the matter component in the lens galaxy, which includes stars and gas<sup>6</sup>. At distances close to the lensing galaxy, these terms can dominate the lensing signal. We assume that the effect of the matter component in the lens galaxy can be considered as a point mass contribution located at the position of the lens galaxy,

$$\Delta\Sigma_*(r_p) = \frac{\tilde{M}_*}{\pi r_p^2}, \quad (22)$$

where  $\tilde{M}_*$  is in units of  $h^{-1}M_\odot$  and the projected radius  $r_p$  is in units of  $h^{-1}$  pc. The stellar population synthesis models (hereafter SPS) infer the stellar mass,  $M_*$  based upon the luminosity and mass-to-light ratio of stars. These masses therefore have the units of  $h^{-2}M_\odot$ , and this stellar mass is related to the baryonic lensing mass by  $\tilde{M}_* = M_*/h$ . Our models adopt the parameter  $\tilde{M}_*$  to allow a comparison of this mass with the stellar mass measurements from the SPS models (see Miyatake et al. 2013, for a more detailed comparison).

In addition to the HOD parameters, our analytical predictions also depend upon the cosmological parameters, via the halo mass function, the halo bias function, and the cosmology dependence of the concentration-mass relation (van den Bosch et al. 2013). There are a number of simulation-calibrated ingredients required to use the analytical expressions in this section. For the sake of completeness and reproducibility, we list each of them below. We assume the halo masses to be 200 times overdense with respect to the background matter density. We use the halo mass function calibration of Tinker et al. (2008) and large scale bias calibration of Tinker et al. (2010) for this particular definition. The radial dependence of halo bias was calibrated by Tinker et al. (2005) for friends-of-friends halos. We use an appropriate modification to take into account the spherical overdensity definition of halos and the effects of halo exclusion (see van den Bosch et al. 2013) which allows us to calculate  $Q(k|M_1, M_2, z)$ . We use a nuisance parameter  $\psi$  to marginalize over the uncertain description of radial dependence of halo bias. This parameter governs the behaviour of the prediction in the transition regime between one halo and the two halo term (see van den

Bosch et al. 2013, for details). The concentration of dark matter halos is assumed to follow the concentration-mass relation calibration presented by Macciò et al. (2008). We allow for a normalization parameter  $R_c$  which characterizes deviations from this fiducial relation and assign it a prior of  $1.00 \pm 0.15$ . We also assume that the satellite galaxies follow the dark matter distribution in an unbiased manner. In addition, we also allow for a 2.5 percent uncertainty in the modelling of the projected clustering signal (the overall amplitude) to account for the inaccuracies of the model. We do not explicitly include a corresponding systematic uncertainty in the lensing calibration, since the statistical errors on that measurement are already sufficiently large that they are the dominant source of error.

#### 4.2. Cosmological parameter dependence of the measurements

The abundance, clustering and the lensing measurements depend upon the fiducial cosmological model,  $C^{\text{fid}}$ , that we have assumed to convert the angular and redshift differences in the positions of galaxies to their comoving separation (see e.g., More 2013). We account for this dependence as follows. For a given cosmological model  $C$ , we multiply the predicted abundance of galaxies  $\bar{n}_g(C)$  in the redshift bin  $[z_2, z_1]$  by the ratio of the comoving volumes

$$\bar{n}'_g = \bar{n}_g(C) \frac{\chi^3(z_2, C) - \chi^3(z_1, C)}{\chi^3(z_2, C^{\text{fid}}) - \chi^3(z_1, C^{\text{fid}})} \quad (23)$$

in order to compare it to abundance measured assuming  $C^{\text{fid}}$ . Here,  $\chi(z)$  denotes the comoving distance to redshift  $z$ . For the clustering and the lensing signals, we first calculate  $w_p$  and  $\Delta\Sigma$  at comoving separations  $r'_p$ , which are related to the projected comoving separation  $r_p^{\text{fid}}$  at which the measurements were performed by

$$r'_p = r_p^{\text{fid}} \left[ \frac{\chi(\bar{z}, C)}{\chi(\bar{z}, C^{\text{fid}})} \right] \quad (24)$$

where  $\chi^{\text{fid}}$  and  $\chi$  denote the comoving distance to the median redshift  $\bar{z}$  in  $C^{\text{fid}}$  and  $C$ , respectively. This calculation accounts for the difference in the conversion of angular differences between galaxies to comoving separations. We need to further change the amplitude of the predictions of both  $w_p$  and  $\Delta\Sigma$ , such that

$$\tilde{w}_p(r_p) = w_p(r'_p) \left[ \frac{E(\bar{z})}{E^{\text{fid}}(\bar{z})} \right] \quad (25)$$

$$\tilde{\Delta\Sigma}(r_p) = \Delta\Sigma(r'_p) \left[ \frac{\Sigma_{\text{crit}}(\bar{z}, z_s)}{\Sigma_{\text{crit}}^{\text{fid}}(\bar{z}, z_s)} \right], \quad (26)$$

where the former equation accounts for the cosmology dependence of the conversion from redshift difference to comoving line-of-sight distances, while the latter corrects for the cosmology dependence of  $\Sigma_{\text{crit}}$ , which is used to calculate the lensing signal from the measured ellipticities. We use a fixed source redshift to calculate  $\Sigma_{\text{crit}}(\bar{z}, z_s)$  due to its weak dependence on the choice of the source redshift. We compare these modified predictions with the measurements. The validity of this procedure to capture the cosmological dependence of the measurements procedure was verified in More (2013).

In summary, the analytical model we use to describe the measurements has 17 parameters. The first set of 5 param-

<sup>6</sup> The gas fractions around high stellar mass galaxies are expected to be small, so we assume all the baryonic mass is in stars.

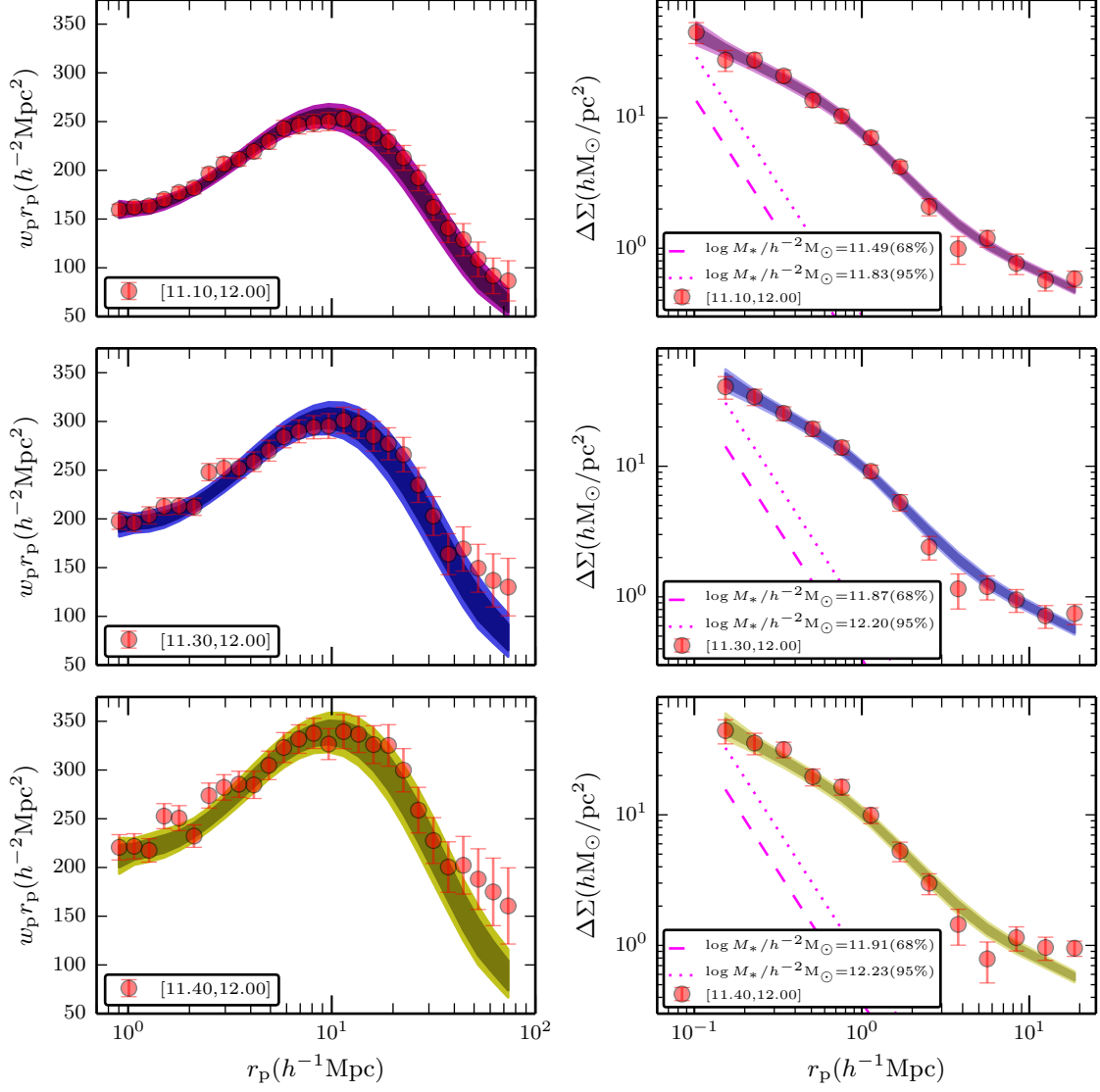


**Figure 9.** The 68 and 95 percent confidence intervals of the fits to the clustering measurements and the lensing measurements from the fiducial sample obtained from the HOD modelling exercise. The intervals are obtained by projecting uncertainties in all the model parameters around the best-fit model. The reduced  $\chi^2$  for the best fit models in the three cases are 0.8, 1.3 and 1.5 for 31, 31 and 30 degrees of freedom, respectively (see text for details).

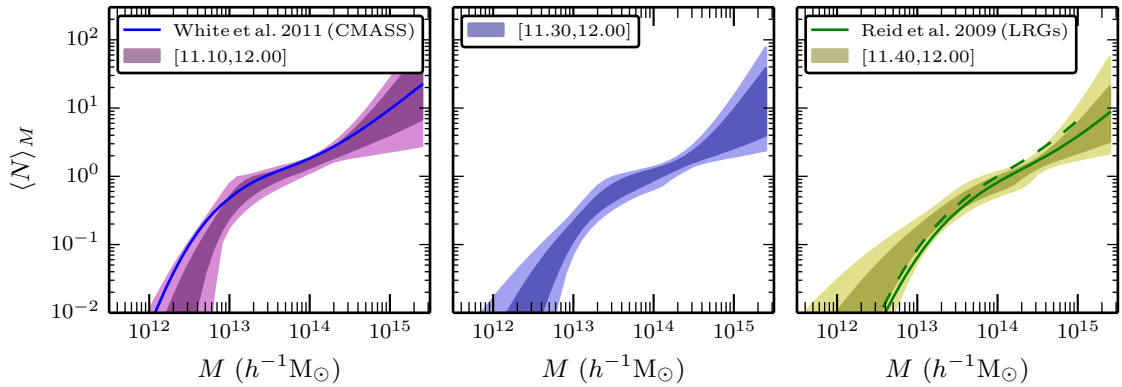


**Figure 10.** The 68 and 95 percent confidence intervals of the halo occupation distribution of CMASS galaxies in samples A, B and C obtained from our modelling exercise are shown in the three different panels, respectively. The HOD constraints displayed here are marginalized over the uncertainty in the cosmological parameters. For HOD constraints at the best fit value of cosmological parameters, see Paper I.

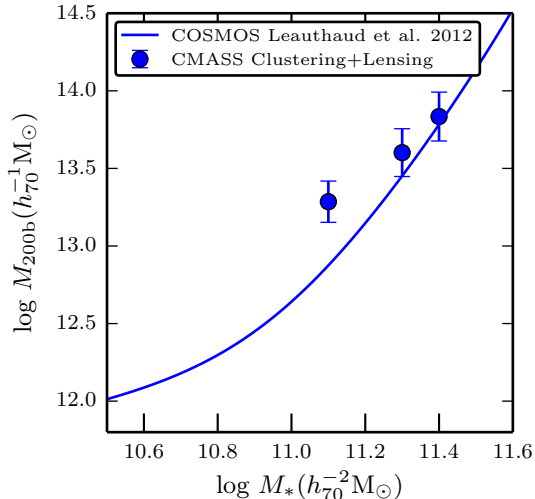


**Figure 11.** The average halo mass of central galaxies in our CMASS subsamples at their respective stellar mass threshold obtained from the HOD analysis. The solid line shows the results of Leauthaud et al. (2012), derived based on a joint clustering and weak lensing analysis using data from the COSMOS survey but using stellar mass binned samples. Differences seen at lower stellar mass between the results in this work and in Leauthaud et al. (2012) are a consequence of the color cuts placed on the CMASS sample (but not on the sample used on that work); see text for details. The higher stellar mass samples are expected to be more complete.

ters,  $M_{\min}$ ,  $\sigma^2$ ,  $M_{\text{sat}}$ ,  $\alpha$ ,  $\kappa$ , describes the halo occupation distribution of galaxies. The parameter  $M_{*,11}$  describes the average stellar mass of galaxies in units of  $h^{-2}M_{\odot}$ , while  $\mathcal{R}_c$  is the normalization of the concentration mass relation with respect to the one obtained from simulations. We have 5 nuisance parameters:  $\psi$ ,  $p_{\text{off}}$ ,  $\mathcal{R}_{\text{off}}$ ,  $\alpha_{\text{inc}}$ ,  $M_{\text{inc}}$ . Finally there are 5 cosmological parameters:  $\Omega_m$ ,  $\sigma_8$ ,  $\Omega_b h^2$ ,  $n_s$  and  $h$ . We let  $\Omega_m$  and  $\sigma_8$  be completely free but use priors on the latter three cosmological parameters from the joint likelihood of the cosmic microwave background analysis of the WMAP 9-year data and the high resolution CMB measurements from the South Pole Telescope (SPT) and the Atacama Cosmology Telescope (ACT) obtained by Hinshaw et al. (2013). We will denote this combination of cosmological priors as WMAP9\_E. Our samples A and B have 27 measurements of  $w_p$ , 14 measurements of  $\Delta\Sigma$  and one of the abundance for the subsample each, used for the analysis. We have 17 total model parameters, with priors on the 3 cosmological parameters ( $\Omega_b h^2$ ,  $n_s$ ,  $h$ ) and on the 3 parameters  $\alpha$ ,  $\mathcal{R}_c$ ,  $\psi$ . Therefore, the total number of degrees of freedom are  $27 + 14 + 1 - 17 + 6 = 31$ . The number of degrees of freedom are 30 for subsample C which does not include the innermost bin in the lensing measurement. We perform a Bayesian inference of cosmological parameters given the measurements using a Markov chain Monte Carlo (hereafter MCMC) analysis. In particular, we use the affine invariant sampler of Goodman & Weare (2010) as implemented by the software *emcee* to navigate the parameter space (Foreman-Mackey et al. 2013).

## 5. RESULTS

We now present the results of our cosmological analysis and the different systematic tests we have performed. The 68 percent confidence intervals on each of our parameters from the analysis of the abundance, clustering and the lensing signal of the three stellar mass subsamples we use are listed in Table 1. The top left- and right-hand panels of Figure 9 show the

projected clustering data and the lensing data with errorbars for the fiducial subsample of galaxies, while the middle and bottom panels display the corresponding results for subsamples B and C, respectively. The dark and light purple shaded regions denote the 68 and 95 percent confidence intervals obtained from the MCMCs, respectively, marginalizing over all of the model parameters. The overall shape of the clustering and lensing signals is reproduced well by the model. The clustering and lensing predictions are able to successfully reproduce the increasing strength with stellar mass thresholds, as in the observations. The model is also able to reproduce the shape of the weak lensing signal and the observed transition between the one- and two-halo regimes. There is a hint that the model has some difficulty reproducing the high amplitude of the clustering on large scales for the higher stellar mass threshold samples. However, note that the large scales have significant covariance. The reduced  $\chi^2$  for the best fit models for the fiducial subsample is 0.8, while those of the subsamples B and C are 1.3 and 1.5, respectively. The probabilities to exceed the  $\chi^2$  values by chance given the number of degrees of freedom are equal to 76%, 10% and 4%, respectively.

The right hand panels of Figure 9 present the 68 and 95 percent upper limits on the average stellar mass of the galaxies in each subsample using dashed and dotted lines, respectively. The 68 percent confidence limits from the weak lensing modelling are  $\log\langle M_* \rangle < 11.49h^{-2}M_{\odot}$ ,  $\log\langle M_* \rangle < 11.87h^{-2}M_{\odot}$  and  $\log\langle M_* \rangle < 11.91h^{-2}M_{\odot}$  for the progressively larger stellar mass subsamples, respectively. These limits on the average stellar masses from weak lensing can be compared to the mean stellar masses obtained from the stellar population synthesis models, as discussed in the companion paper (Miyatake et al. 2013).

The constraints on the halo occupation distribution for the three samples are shown in Figure 10. As expected, the HOD shifts to higher halo masses for subsamples B and C. The scatter in halo masses increases significantly for the highest threshold sample. A constant scatter in stellar masses at fixed halo mass translates into an increasing scatter in halo masses at fixed stellar mass due to the shallow power law index of the stellar mass halo mass relation at the massive end (see e.g., More et al. 2009a). We compare our HOD constraints to those obtained by White et al. (2011) for the full sample of CMASS galaxies in the left hand panel of Figure 10. Compared to their sample, our fiducial subsample of galaxies resides in slightly larger halo masses owing to our subsample selection which removes low stellar mass galaxies. Next we compare the HOD of our subsample C to that of luminous red galaxies (LRGs) from SDSS-I/II at  $z \sim 0.3$ . These two samples have comparable number densities. In the right hand panel, we compare the HOD constraints with those obtained by Reid & Spergel (2009) for luminous red galaxies shown with solid line. The comparison demonstrates the similarity in the HOD of the two samples. For reference, we also show the HOD of LRGs shifted to adjust for the difference in the mass of the halos owing to the difference in the average redshift of the LRG sample ( $z \sim 0.3$ ) and that of our subsample ( $z \sim 0.53$ ). This particular HOD should hold if all LRGs have both maintained their identities (central or satellite) inside their respective halos and if none of these halos merged with each other in the redshift interval  $z \in [0.35, 0.57]$ .

The clustering and lensing signals of satellite galaxies are different from that of central galaxies on small scales. Therefore it is important to obtain a good estimate on the fraction of galaxies that are satellites in our subsamples in order to cor-

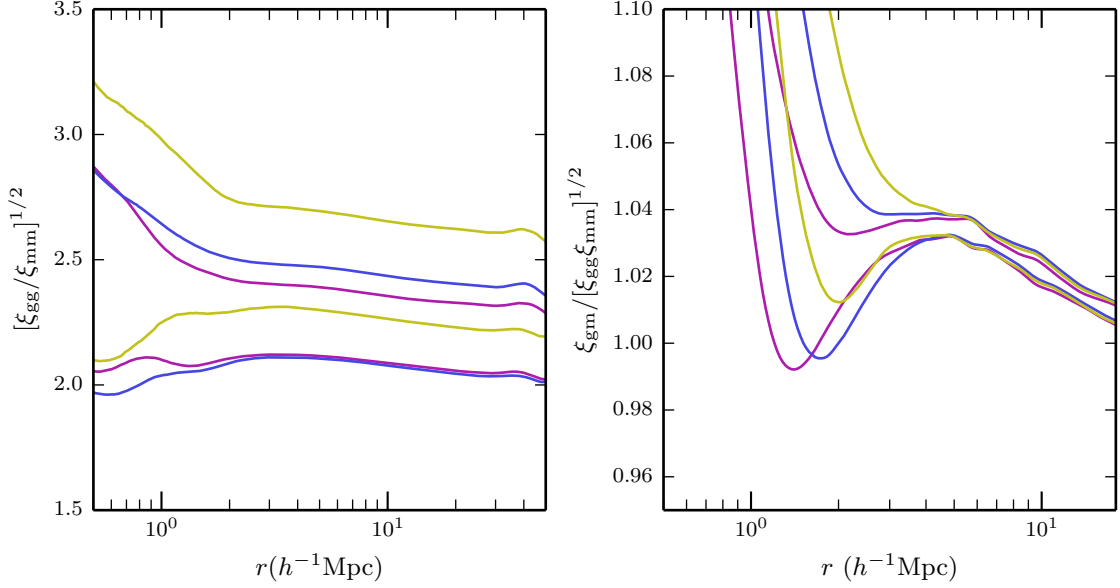


**Figure 12.** The 68 percent confidence limits on the scale-dependence of bias (left panel) and the cross-correlation coefficient (right panel) of our subsamples A, B and C are enclosed by the magenta, blue and yellow lines, respectively. The bias tends to a constant value on large scales, and the cross-correlation coefficient shows small but significant deviations from unity at small scales.

rectly interpret the measurements. The satellite fraction of our fiducial subsample is  $8.3 \pm 3.1$  percent. This value is consistent with the satellite fraction quoted by White et al. (2011),  $10 \pm 2$  percent, albeit on the lower side. This is not entirely unexpected as our subsample excludes the low stellar mass galaxies in the entire CMASS sample that was used by White et al. (2011). The satellite fraction is expected to decrease as a function of stellar mass. The satellite fractions in our higher stellar mass threshold subsamples are  $6.8 \pm 2.6$  and  $4.6 \pm 2.1$ , respectively, consistent with this expectation.

The large-scale effective bias of galaxies (defined as in Equation 7) of our fiducial subsample of galaxies is constrained to be  $2.15 \pm 0.13$ . The galaxy bias systematically increases to  $2.26 \pm 0.17$  and  $2.54 \pm 0.19$ , respectively, for subsamples with progressively larger stellar mass thresholds. In the left hand panel of Figure 12, we show the scale dependence of the bias defined as

$$b(r) = \left[ \frac{\xi_{gg}(r)}{\xi_{mm}(r)} \right]^{1/2}, \quad (27)$$

where  $\xi_{gg}$  and  $\xi_{mm}$  are the three dimensional galaxy and matter correlation functions, respectively. The magenta, blue and yellow lines enclose the 68 percent confidence intervals for our subsamples A, B and C after marginalizing over all of our model parameters, respectively. The right hand panel shows the cross-correlation coefficient defined as

$$r_{cc}(r) = \frac{\xi_{gg}(r)}{[\xi_{mm}(r)\xi_{gm}(r)]^{1/2}}, \quad (28)$$

where  $\xi_{gm}(r)$  is the three dimensional galaxy-matter cross-correlation. The cross-correlation coefficient is larger than one on small scales (see e.g., Seljak 2000b), but tends to unity on large scales. This behaviour of the cross-correlation coefficient on large scales can be used to obtain the matter correlation function directly from observations of the galaxy clustering and galaxy-galaxy lensing on large scales (Seljak 2000b;

Guzik & Seljak 2001; Baldauf et al. 2010; Mandelbaum et al. 2013).

The HOD constraints we obtained from our analysis allows calculation of the average halo mass at the stellar mass threshold of each of our subsamples. These results are displayed as points with errorbars in Figure 11. The solid lines show the average stellar mass halo mass relation obtained from a similar analysis of the abundance, clustering and lensing signal from COSMOS (Leauthaud et al. 2012). The COSMOS sample covers a much smaller area on the sky but is expected to be more stellar mass complete compared to the CMASS sample, which has color cuts designed to select the luminous red galaxy population. The comparison shows that the galaxies in the fiducial subsample on average reside in slightly larger halo masses at fixed stellar mass than the results from COSMOS. This result is consistent with the expectation that massive redder galaxies reside in higher mass halos on average (see e.g., More et al. 2011). The results for subsamples B and C are, however, consistent with the results from COSMOS, implying that the incompleteness in our subsamples becomes smaller for the larger stellar mass thresholds. As the blue fraction of galaxies decreases steeply as a function of stellar mass, the CMASS colour selection no longer biases the sample. Tinker et al. (in preparation) demonstrate this trend of decreasing incompleteness with increasing stellar mass threshold in the CMASS sample based on galaxies that did not pass the CMASS colour cuts but were observed as part of an SDSS-III ancillary program (J. Tinker, priv. comm.).

We show the posterior distributions of our cosmological constraints as histograms in the diagonal panels of Figure 13 for our fiducial subsample. The shaded regions highlight the degeneracies between the cosmological parameters. The distributions shown by the blue solid lines denote the priors that we have assumed on the auxiliary cosmological parameters  $\Omega_b h^2$ ,  $n_s$  and  $h$  based on the analysis of WMAP9+SPT+ACT (Hinshaw et al. 2013). There is no significant improvement on these parameters with the addition of our data, neither does our data shift the posteriors of these parameters away from the

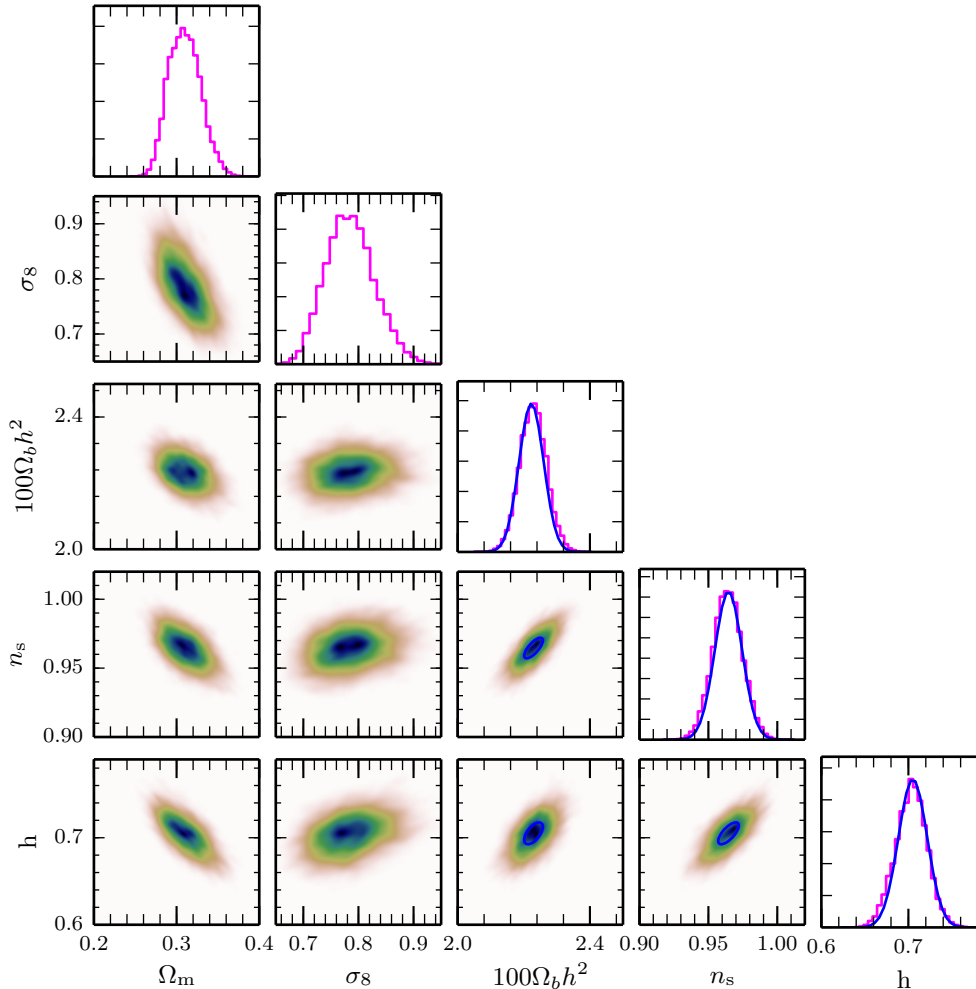


**Figure 13.** The degeneracies between different cosmological parameters as inferred from the analysis of the clustering and lensing signal from our fiducial subsample A are shown with shaded contours in the off-diagonal panels. The magenta histograms in the diagonal columns represent the posterior distribution of each of our cosmological parameters. The blue distributions in the diagonal panels and the blue contour (68 percent confidence) in some of the off-diagonal panels represent the prior information we adopt on the parameters  $[\Omega_b h^2, n_s, h]$ .

priors (cf. Cacciato et al. 2013a). We also observe the degeneracy in the constraints on  $\Omega_m$  and  $\sigma_8$  that we anticipated from our theoretical considerations: a larger value of  $\Omega_m$  prefers a model with smaller value of  $\sigma_8$  as implied from Figure 7.

The cosmological constraints on  $\Omega_m$  and  $\sigma_8$  obtained from the three stellar mass subsamples analysed in this paper are depicted in Figure 14 with magenta, blue and yellow contours, respectively. The constraints from our higher threshold subsamples, which are expected to be more complete, are consistent with the fiducial subsample<sup>7</sup>. Thus, although the fiducial subsample may have been incomplete, this incompleteness does not cause significant biases in the cosmological constraints, compared to the current statistical precision. Given that the HOD for each of the subsamples differs significantly from each other, this agreement is non-trivial.

In our analysis, we have analysed the measurements of clus-

tering to  $r_p > 0.85 h^{-1} \text{Mpc}$ . We tested for additional systematics by extending our measurements to even smaller scales  $r_p > 0.5 h^{-1} \text{Mpc}$ , but restrict ourselves above the fiber collision scale at the highest redshift of our subsamples. The small-scale clustering signal is sensitive to the satellite fraction, and thus our constraints are expected to marginally improve. The 68 and 95 percent confidence levels on  $\Omega_m - \sigma_8$  for such an analysis of our fiducial subsample are compared to those obtained when analyzing the larger scale measurements in Figure 15. This test also does not reveal any significant biases.

The overlap between the CFHT region and the BOSS region consists of only  $100 \text{ deg}^2$ . Therefore, sample variance for the lensing signal is a legitimate concern for our lensing analysis. The CFHT region consists of three different fields which are well separated from one another. The effect of super-survey modes that can affect the measurement is smaller in this case than when the survey area is contiguous (Takada & Hu 2013). Regardless, if the CFHT region happens to represent a relatively under or over-dense part of the Universe, then there are a number of ways in which our analysis could be affected.

First, the number density of galaxies in the particular patch

<sup>7</sup> A quantitative measure of the consistency would require an analysis of the clustering and lensing measurements of all subsamples together including the correlation between the subsamples. This investigation is beyond the scope of this work. The large overlap in the 68 and 95 percent confidence levels suggests there exists cosmological parameter space which can simultaneously explain the measurements in each of the subsample.

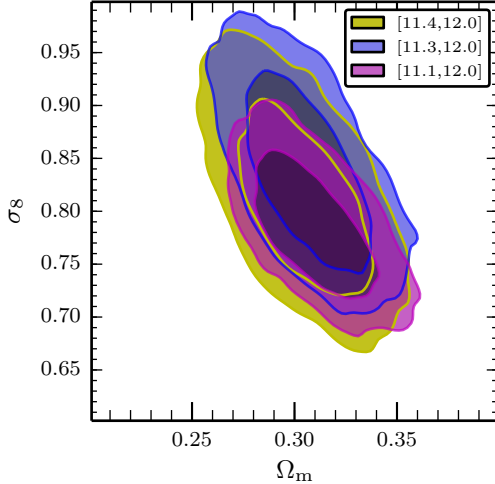


**Figure 14.** The constraints in the  $\Omega_m - \sigma_8$  plane obtained from the analysis of the different stellar mass threshold samples are shown using contours of different colours. As the higher stellar mass subsamples are expected to be more complete, this provides a systematic check of the possible bias in our cosmological constraints due to incompleteness.

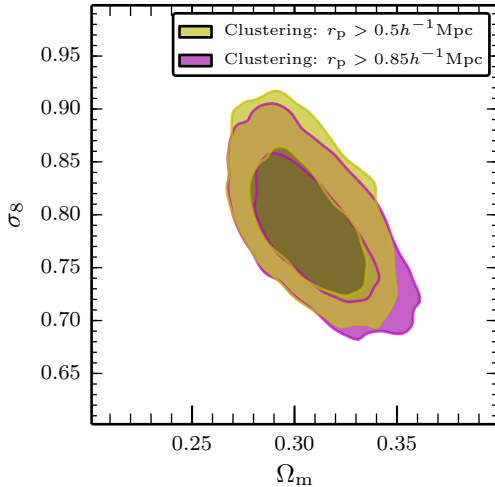


**Figure 15.** The constraints in the  $\Omega_m - \sigma_8$  plane obtained from the fiducial subsample A, but restricting the projected clustering signal to different scales. The magenta contours correspond to our fiducial analysis with  $r_p > 0.85 h^{-1} \text{Mpc}$ , while the yellow contours correspond to  $r_p > 0.5 h^{-1} \text{Mpc}$ . Inclusion of the small scale clustering information does not cause a drastic improvement in the cosmological constraints.

could be affected. This change has a relatively minor effect on the lensing signal, since the signal is normalized by the total number of galaxies (see the factors  $\mathcal{H}_x$  in Equations 13-14). Second, the concentration of halos can depend upon the environment (see e.g., Macciò et al. 2007), so the halos of the lensing galaxies could have density profiles which deviate from their expected median. In this case, the nuisance parameter,  $\mathcal{R}_c$ , that we adopt should be able to marginalize over this uncertainty. The third possibility is that the two-halo term of the lensing contribution is affected in these regions (see e.g., Gao & White 2007). To explore the impact of this possibility, we removed all lensing information from scales above  $2.6 h^{-1} \text{Mpc}$  for our fiducial subsample where the two-halo term is expected to be dominant. The resulting cos-

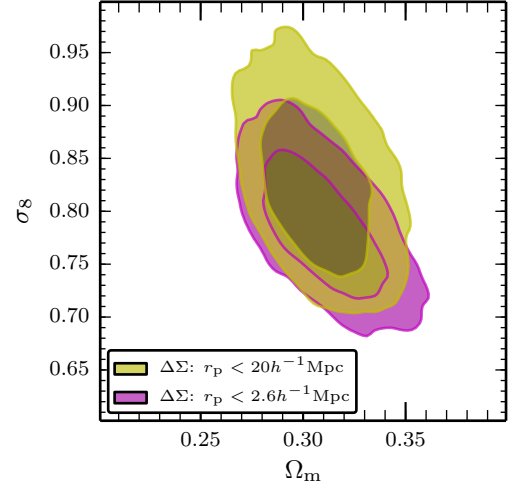


**Figure 16.** The constraints in the  $\Omega_m - \sigma_8$  plane obtained from the fiducial subsample A, but restricting the galaxy-galaxy lensing signal to small scales. The magenta contours correspond to our fiducial analysis with  $r_p < 20.0 h^{-1} \text{Mpc}$ , while the yellow contours correspond to  $r_p < 2.6 h^{-1} \text{Mpc}$ . By excluding the large scales, we are less sensitive to the two halo-term in the lensing signal, which could be affected if the CFHT sample is not representative of our CMASS subsample.

mological constraints and their comparison with our fiducial analysis is shown in Figure 16. As expected, the errorbars are larger when we restrict our analysis to small scales. Although there is a slight tendency toward larger  $\Omega_m$  and  $\sigma_8$  values, both the 68 and the 95 percent confidence levels overlap to a large extent. Finally for completeness, we mention that it could be possible that galaxy formation is heavily dependent on the local cosmological parameters, and this could affect our analysis. However, a proper study of this issue is beyond the scope of this paper. All of these effects can be remedied by surveying larger portions of the sky.

In Figure 17, we compare the cosmological constraints on  $\Omega_m$  and  $\sigma_8$  from our fiducial subsample with the results obtained by a variety of other complementary methods. The 68 and 95 percent confidence intervals obtained by the CMB temperature fluctuation power spectrum measurements of WMAP9 (Hinshaw et al. 2013) in combination with the high-multipole measurements of the same from SPT (Keisler et al. 2011) and ACT (Das et al. 2011) are shown as green shaded regions and denoted as WMAP9.E. The chrome yellow shaded regions show the confidence intervals obtained by the Planck collaboration using the temperature power spectrum measurements (Planck Collaboration et al. 2013b). The grey bands correspond to the 68 and 95 percent confidence constraints obtained by Planck (Planck Collaboration et al. 2013e) but using the thermal Sunyaev-Zel'dovich (SZ) power spectrum measurements (Sunyaev & Zeldovich 1972, for the SZ effect), while the brown shaded regions denote the constraints obtained from Planck SZ cluster abundances (Planck Collaboration et al. 2013d). The confidence contours obtained by performing a joint analysis of the abundance, clustering and lensing signals of the SDSS main sample of galaxies carried out by Cacciato et al. (2013a) are shown using dark blue contours, while the constraints obtained by Mandelbaum et al. (2013), using a joint analysis of clustering and lensing but focusing on large scales, are shown as yellow contours. The light blue shaded regions correspond to the analysis of the tomographic weak lensing signal from CFHTLenS by Hey-

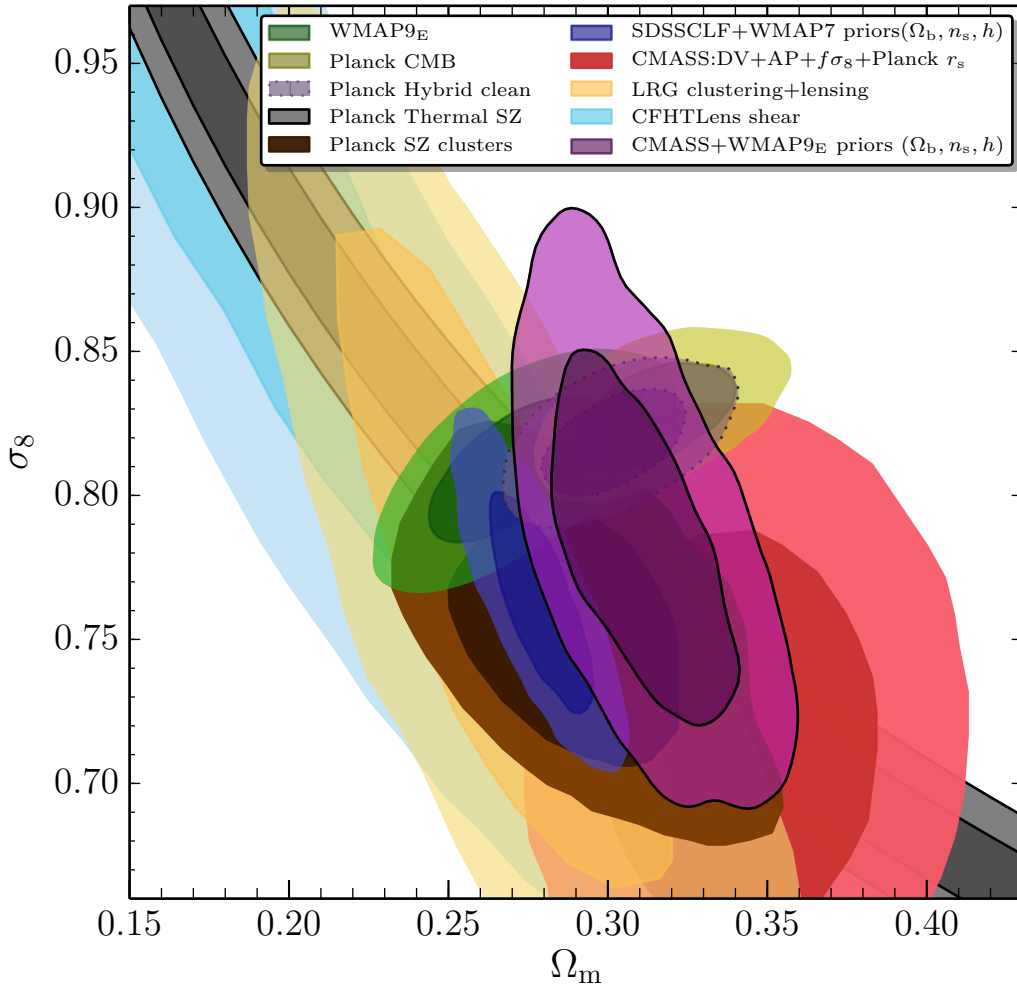


**Figure 17.** The 68 and 95 percent confidence constraints on the matter density parameter,  $\Omega_m$  and the fluctuation amplitude parameter,  $\sigma_8$  obtained from the analysis of the clustering and lensing measurements of our fiducial sample are shown using magenta contours. These can be compared with results from other cosmological probes such as the analyses of the cosmic microwave background carried out by the WMAP team (green shaded regions), the Planck team (chrome yellow shaded regions) and a reanalysis of Planck data by Spergel et al. (2013, violet regions with dotted contours), the SZ cluster abundances (brown shaded regions) and the thermal SZ power spectrum (grey shaded regions) carried out by the Planck team, the joint analysis of clustering and lensing of the SDSS main galaxy sample (dark blue), and that of the LRG sample (yellow), the joint analysis of redshift space distortions, BAOs and the Alcock Paczynski test using CMASS galaxies (red shaded regions) and the tomographic weak lensing signal (light blue shaded regions). The figure shows that our results are consistent, complementary and competitive with constraints from different cosmological probes.

mans et al. (2013). The red shaded confidence regions are the results of Beutler et al. (2013), obtained by combining the baryon acoustic oscillation measurements (assuming the Planck value for the sound horizon)<sup>8</sup>, the redshift space distortions and the Alcock-Paczynski test (Alcock & Paczynski 1979) from the CMASS galaxy sample.

The two results from the cosmic microwave background (WMAP9\_E and Planck) are in agreement, although there is a noticeable difference in the central values obtained from the analysis by the two teams. The WMAP9\_E analysis prefers a lower value for both  $\Omega_m$  and  $\sigma_8$  compared to the Planck analysis. Our confidence regions overlap with both WMAP9\_E and Planck, and roughly lie in an orthogonal direction. This results demonstrates that our constraints are complementary to those obtained from the CMB analyses.

The measurements from the thermal SZ power spectrum and the SZ cluster abundances from Planck are also consistent

<sup>8</sup> The contours shift to the right by  $\sim 2-\sigma$  if the value of the sound horizon from WMAP9 is assumed.

with each other and with the WMAP9\_E and Planck CMB analysis. However, at the central value of  $\Omega_m$  preferred by Planck, both these analyses prefer a much lower value of  $\sigma_8$ . The same tendency for the preference of a lower value of  $\sigma_8$  at the central value of  $\Omega_m$  preferred by Planck is also seen in our results as well as those from the SDSS conditional luminosity function (CLF) analysis of Cacciato et al. (2013a), LRG clustering and weak lensing analysis of Mandelbaum et al. (2013), the CFHTLenS tomographic weak lensing analysis of Heymans et al. (2013) and the redshift space distortion (RSD) measurements of Beutler et al. (2013). However, there is a common region of overlap between the different analyses: this common region suggests slightly smaller (larger) values of both  $\Omega_m$  and  $\sigma_8$  compared to Planck (WMAP9\_E) CMB constraints. Interestingly, the results from a reanalysis of the Planck data using a different foreground cleaning procedure performed by Spergel et al. (2013, shown using dotted contours) also results in constraints in the same overlapping region. The more recent BAO analyses also hint towards an



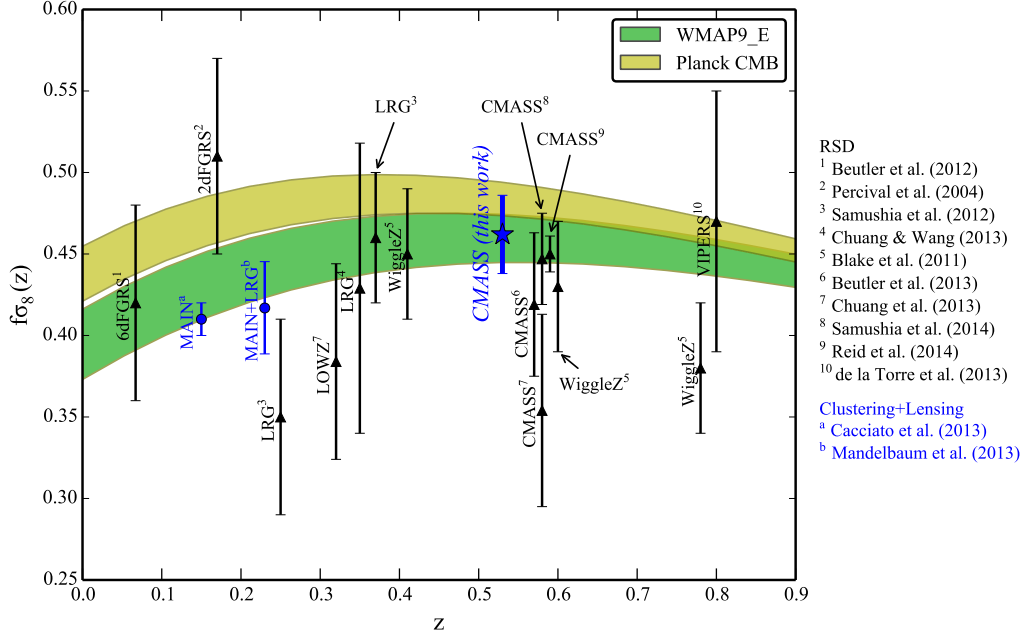


**Figure 18.** Blue dots denote  $f\sigma_8(z)$  constraints calculated from our measurement and other joint analyses of clustering and lensing measurements. Black triangles denote  $f\sigma_8(z)$  constraints based on various RSD measurements. Some of the RSD CMASS measurements are shifted along the redshift-axis for clarity (+0.01 for references 6 and 8 and +0.02 for reference 9). Error bars show 68 percent confidence level. Green (Yellow) shaded region shows  $f\sigma_8$  predictions with 68 percent confidence intervals based on the WMAP9 (Planck) CMB measurement. Our result is the highest redshift cosmological analysis using a joint analysis of the clustering and lensing signal of galaxies.

intermediate value for  $\Omega_m$  in between WMAP9 and Planck (Anderson et al. 2014). Our results are also consistent with constraints from the cross-correlation of the thermal Sunyaev Zéldovich signal from Planck with the gravitational lensing potential (Hill & Spergel 2014) and with the X-ray cluster map from ROSAT (Hajian et al. 2013), both of these analyses also prefer intermediate values of the parameters  $\Omega_m$  and  $\sigma_8$ .

In Figure 18, we present constraints on  $f\sigma_8(z)$ , where  $f = -d \ln D(z)/d \ln(1+z)$  is the logarithmic growth rate and  $\sigma_8(z) = \sigma_8 D(z)/D(0)$  is the linear matter fluctuation at redshift  $z$ , that are calculated from our measurement and other joint analyses of clustering and lensing measurements (Cacciato et al. 2013a; Mandelbaum et al. 2013). We also show the confidence regions for a  $\Lambda$ CDM model assuming cosmological parameters from WMAP9.E and Planck using green and chrome yellow shaded bands. Our measurement is at the highest redshift among the clustering and lensing joint analyses and is consistent with these measurements and the WMAP9.E and Planck predictions. For comparison, we have also compiled various RSD measurements (Percival et al. 2004; Blake et al. 2011b; Samushia et al. 2012; Beutler et al. 2012; Chuang et al. 2013; de la Torre et al. 2013; Chuang & Wang 2013; Beutler et al. 2013; Samushia et al. 2014; Reid et al. 2014). Our measurement is also largely consistent with the RSD measurements.

In our modelling exercise we have assumed that the halo mass of a galaxy has the dominant effect in determining its properties. Our halo occupation distribution formalism assumes that the halos of a given mass which host the galaxies from our subsamples are a random subsample of halos of that particular mass. It assumes that the presence or absence of a galaxy is not determined by the assembly history of the halo. The extent to which this assumption holds is, however, unclear. It is important to note that our parent galaxy sample is designed to select galaxies based on colour. Recently,

subhalo abundance matching methods have been extended to assign both stellar mass and colours to galaxies in mock catalogs (Hearin & Watson 2013). Their methods are based on the simple idea that properties of galaxies such as their colour or star formation rate may depend on the formation age of the halo defined in a suitable manner. These models have been successfully employed to qualitatively match the colour-dependent clustering of galaxies and the galaxy-galaxy lensing signal (Hearin et al. 2013). Such mock galaxy catalogs by construction have assembly bias. In such cases, halo age in addition to the mass decides the colour of galaxies.

If such models reflect the true nature of galaxy formation in the Universe, then the selection applied to determine our parent galaxy sample (CMASS selection) may identify galaxies at a given fixed halo mass that preferentially live in halos which formed earlier (see e.g., Zentner et al. 2013, for a discussion of the effect in the SDSS main galaxy sample). It is well known that the clustering of halos at fixed halo mass depends upon the formation age of the halo: halos that form earlier cluster more strongly than average (Gao & White 2007), which can be problematic for our inference of cosmological parameters from the halo mass-bias relation. However, it is also known that the difference in the formation time-dependent clustering of halos is less pronounced at the high mass end. For halos that form from the initial peaks with height  $\nu > 1.8$ , the formation age dependence is negligible. The fiducial subsample used in our analysis has a bias  $b = 2.15 \pm 0.13$ , which corresponds to peak heights  $\nu \sim 2.0$ . The high value of peak height limits the impact that assembly bias can have on our results. Nevertheless, a more thorough study of how assembly bias properties other than the formation history, e.g. the spin of halos, their concentrations, etc. can affect our results is warranted.

In addition, the theoretical foundation of our results are the calibrations of the matter density distributions from collision-

**Table 1**  
Posterior distribution of parameters from the MCMC analysis

Parameter	Subsample		
	[11.10,12.00]	[11.30,12.0]	[11.40,12.0]
$\log M_{\min}$	$13.13^{+0.13}_{-0.13}$	$13.45^{+0.15}_{-0.15}$	$13.68^{+0.16}_{-0.16}$
$\sigma^2$	$0.22^{+0.14}_{-0.15}$	$0.45^{+0.24}_{-0.25}$	$0.79^{+0.41}_{-0.39}$
$\log M_1$	$14.21^{+0.11}_{-0.13}$	$14.51^{+0.17}_{-0.15}$	$14.56^{+0.27}_{-0.22}$
$\alpha$	$1.13^{+0.38}_{-0.45}$	$1.14^{+0.47}_{-0.51}$	$1.00^{+0.45}_{-0.43}$
$\kappa$	$1.25^{+0.71}_{-0.69}$	$0.85^{+0.67}_{-0.67}$	$1.19^{+0.99}_{-0.96}$
$M_{*,11}$	$0.0^{+3.1}$	$0.0^{+7.3}$	$0.0^{+8.1}$
$\mathcal{R}_c$	$0.98^{+0.19}_{-0.20}$	$1.01^{+0.20}_{-0.19}$	$1.02^{+0.21}_{-0.22}$
$\psi$	$0.93^{+0.14}_{-0.13}$	$0.93^{+0.15}_{-0.14}$	$0.94^{+0.15}_{-0.14}$
$p_{\text{off}}$	$0.34^{+0.18}_{-0.18}$	$0.37^{+0.24}_{-0.21}$	$0.36^{+0.19}_{-0.19}$
$\mathcal{R}_{\text{off}}$	$2.2^{+1.5}_{-1.3}$	$2.3^{+1.5}_{-1.5}$	$2.4^{+1.4}_{-1.4}$
$\alpha_{\text{inc}}$	$0.44^{+0.35}_{-0.34}$	$0.53^{+0.25}_{-0.24}$	$0.57^{+0.20}_{-0.18}$
$\log M_{\text{inc}}$	$13.57^{+0.32}_{-0.30}$	$13.88^{+0.33}_{-0.30}$	$14.08^{+0.32}_{-0.29}$
$\Omega_m$	$0.310^{+0.019}_{-0.020}$	$0.306^{+0.021}_{-0.020}$	$0.304^{+0.022}_{-0.021}$
$\sigma_8$	$0.785^{+0.044}_{-0.044}$	$0.839^{+0.061}_{-0.061}$	$0.813^{+0.060}_{-0.059}$
$100\Omega_b h^2$	$2.228^{+0.040}_{-0.040}$	$2.226^{+0.040}_{-0.039}$	$2.222^{+0.041}_{-0.041}$
$n_s$	$0.964^{+0.011}_{-0.011}$	$0.963^{+0.011}_{-0.010}$	$0.961^{+0.011}_{-0.011}$
$h$	$0.703^{+0.018}_{-0.018}$	$0.700^{+0.017}_{-0.016}$	$0.695^{+0.017}_{-0.017}$

The three columns list the 68% confidence intervals on the model parameters for the three stellar mass subsamples we use in our analysis. The parameter  $M_{*,11}$  denotes the stellar mass in units of  $10^{11} h^{-2} M_{\odot}$  and the 68% limit we quote is a one-sided upper limit.

less numerical simulations. Baryonic processes such as radiation pressure feedback, feedback from supernovae and active galactic nuclei, which are implemented in large volume hydrodynamical simulations, can have a significant effect on the matter power spectrum, the halo mass function and the halo bias functions (Gnedin et al. 2004; Rudd et al. 2008; Cui et al. 2012; Velliscig et al. 2014; van Daalen et al. 2014; Vogelsberger et al. 2014). These consequences are a result of the redistribution of matter in and around halos due to the baryonic feedback effects. The magnitude of the difference is however very dependent on the details of the feedback mechanisms implemented. Our inclusion of the weak prior on the amplitude of the concentration-mass relation (instead of complete reliance on the simulation calibrated normalization) can partially account for a variation in the matter density within halos that could be a result of baryonic effects (see e.g., Zentner et al. 2013). Nevertheless, the impact of baryonic effects is certain to remain a subject of active research in the near future.

## 6. SUMMARY AND FUTURE OUTLOOK

Galaxies are biased tracers of the matter density distribution. Galaxy bias is often treated as a nuisance parameter to be marginalized over in order to use the two-point functions of galaxies to derive cosmological parameters. The origin of galaxy bias is, however, in the special positions that galaxies occupy in the matter density field. Galaxies form within halos which are located at the peaks of the density distribution. They share the bias of the halos in which they reside. The dependence of halo bias on mass is governed by cosmological parameters. Therefore, measurements of the clustering amplitude of galaxies, in combination with the halo masses of galaxies, can turn the nuisance of galaxy bias into a powerful probe of cosmological parameters. In this paper, we utilized such measurements in order to constrain the halo occupation distribution of galaxies as well as the cosmological param-

eters  $\Omega_m$  and  $\sigma_8$ .

For this purpose, we used spectroscopic galaxies from the SDSS-III BOSS project which span an area of about 8500 deg<sup>2</sup> in the sky. From this parent sample, we constructed a subsample of galaxies so that it obeyed stellar mass limits ( $\log M_*/h_{70}^{-2} M_{\odot} \in [11.10, 12.0]$ ) and was approximately complete within the redshift range  $z \in [0.47, 0.59]$ , with an approximately constant abundance. This subsample of galaxies was used to measure the projected galaxy clustering signal with a signal-to-noise ratio of 56 for scales  $0.85 h^{-1} \text{Mpc} < r_p < 80.0 h^{-1} \text{Mpc}$ . We made use of the publicly available galaxy shape and photometric redshift catalogs compiled by the CFHTLenS collaboration based on deeper, higher quality imaging data from the CFHTLS. This imaging catalog had an overlap of a mere 100 deg<sup>2</sup> with the BOSS footprint, but it allowed measurement of the weak gravitational lensing signal of BOSS galaxies with a signal-to-noise ratio of 26 for scales  $0.1 h^{-1} \text{Mpc} < r_p < 20.0 h^{-1} \text{Mpc}$ . To test for systematics arising from our sample selection we also measured the clustering and lensing signals for two other subsamples within the same redshift range, but with larger thresholds in stellar mass  $\log M_*/h_{70}^{-2} M_{\odot} \in [11.30, 12.0]$  and  $\log M_*/h_{70}^{-2} M_{\odot} \in [11.40, 12.0]$ , respectively.

We analyzed these measurements in the framework of the halo model. Our halo model uses a number of ingredients for which the cosmological dependence has been calibrated using numerical simulations, e.g., the halo mass function, the halo bias function, the density profile of halos, the radial dependence of the halo bias. We also utilize well-tested prescriptions to implement halo exclusion and correct for residual redshift space distortion effects in the projected clustering signal due to the use of finite line-of-sight integration limit while projecting the clustering signal. In addition, we also allow for a baryonic component at the center of halos, use parameters to describe the potential incompleteness in the sample, as well as parameters which allow a fraction of central galaxies to be offset from the true center of the halo. We performed an MCMC analysis to obtain the posterior distributions of all our model parameters of interest given our measurements and after marginalizing over all of the nuisance parameters. Our analytical model consists of 17 parameters in total, 5 describing the halo occupation distribution of galaxies, 1 for the stellar mass contribution, 1 for the concentration-mass relation normalization, 5 nuisance parameters, the cosmological parameters,  $\Omega_b h^2$ ,  $n_s$ ,  $h$  with WMAP9+SPT+ACT priors, and  $\Omega_m$  and  $\sigma_8$  were left completely free.

Our model is successful in reproducing the abundance, the projected clustering and the galaxy-galaxy lensing signal in our fiducial subsample as well as the larger threshold stellar mass subsamples. We obtained constraints on the halo occupation distribution parameters of galaxies in each of our subsamples and the cosmological parameters  $\Omega_m$  and  $\sigma_8$ . We compared the stellar mass versus halo mass relation obtained from our analysis with that obtained by Leauthaud et al. (2012) and found that our fiducial subsample may be biased towards high mass halos at the stellar mass threshold of our subsample. However, this bias declines substantially for the larger threshold subsamples. Nevertheless, the cosmological constraints from the analysis of each of the subsamples are in agreement with each other, and reveal no significant biases in the cosmological parameter estimates given the current errors.

The cosmological constraints from the analysis of our fiducial subsample yield  $\Omega_m = 0.310^{+0.019}_{-0.020}$  and  $\sigma_8 = 0.785 \pm$

0.044. This is in excellent agreement with constraints obtained by a number of different studies, including CMB temperature fluctuation power spectrum measurements from WMAP9+SPT+ACT, Planck, and other independent constraints from SZ cluster abundances, SZ thermal power spectrum measurements, cosmic shear measurements and baryon acoustic oscillation measurements combined with redshift space distortions and the Alcock Paczynski test. Furthermore, our results are also consistent with those obtained by a joint analysis of the clustering and lensing of galaxies of the SDSS main sample of galaxies and those of LRGs.

Our analysis extends the redshift at which cosmological constraints have been obtained using a joint clustering and lensing analysis to  $z = 0.53$ . In the near future, the Subaru Hyper Suprime-Cam survey, which began in the spring of 2014, is expected to provide deeper and better quality imaging in the SDSS-III BOSS footprint, extending the overlap region by more than an order of magnitude to an unprecedented  $1400 \text{ deg}^2$ . This will allow a more detailed study of the galaxy-dark matter connection of the BOSS galaxies, and allow division of the sample into finer redshift and stellar mass bins. Analyses such as these with a larger redshift lever arm have the potential to provide complementary and competitive constraints on cosmological models with an extended parameter set such as those with an evolving dark energy equation of state (e.g., Oguri & Takada 2011).

#### ACKNOWLEDGMENTS

SM and MT were supported by World Premier International Research Center Initiative (WPI Initiative), MEXT, Japan, by the FIRST program “Subaru Measurements of Images and Redshifts (SuMIRe)”, CSTP, Japan. HM was supported by Japan Society for the Promotion of Science (JSPS) Postdoctoral Fellowships for Research Abroad and JSPS Research Fellowships for Young Scientists. RM was supported by the Department of Energy Early Career Award program. MT was supported by Grant-in-Aid for Scientific Research from the JSPS Promotion of Science (No. 23340061 and 26610058). DNS acknowledges support from NSF grant AST1311756 and NASA ATP grant NNX12AG72G. SM would like to thank Naoshi Sugiyama for kindly allowing the use of the computing cluster COSMOS at the Physics Department of the University of Nagoya for the analysis presented in this paper. SM is also grateful to Saga Shohei for the administrative support in this regard. The authors would like to thank Ramin Skibba, David Hogg and Marcello Cacciato for useful comments on an earlier version of the paper.

Funding for SDSS-III has been provided by the Alfred P. Sloan Foundation, the Participating Institutions, the National Science Foundation, and the U.S. Department of Energy Office of Science. The SDSS-III web site is <http://www.sdss3.org/>.

SDSS-III is managed by the Astrophysical Research Consortium for the Participating Institutions of the SDSS-III Collaboration including the University of Arizona, the Brazilian Participation Group, Brookhaven National Laboratory, University of Cambridge, Carnegie Mellon University, University of Florida, the French Participation Group, the German Participation Group, Harvard University, the Instituto de Astrofísica de Canarias, the Michigan State/Notre Dame/JINA Participation Group, Johns Hopkins University, Lawrence Berkeley National Laboratory, Max Planck Institute for Astrophysics, Max Planck Institute for Extraterrestrial Physics, New Mexico State University, New York University, Ohio State Univer-

sity, Pennsylvania State University, University of Portsmouth, Princeton University, the Spanish Participation Group, University of Tokyo, University of Utah, Vanderbilt University, University of Virginia, University of Washington, and Yale University.

This work is based on observations obtained with MegaPrime/MegaCam, a joint project of CFHT and CEA/IRFU, at the Canada-France-Hawaii Telescope (CFHT) which is operated by the National Research Council (NRC) of Canada, the Institut National des Sciences de l’Univers of the Centre National de la Recherche Scientifique (CNRS) of France, and the University of Hawaii. This research used the facilities of the Canadian Astronomy Data Centre operated by the National Research Council of Canada with the support of the Canadian Space Agency. CFHTLenS data processing was made possible thanks to significant computing support from the NSERC Research Tools and Instruments grant program.

#### REFERENCES

- Abazajian, K. N., et al. 2009, *ApJS*, 182, 543  
 Ahn, C. P., et al. 2012, *ApJS*, 203, 21  
 Aihara, H., et al. 2011, *ApJS*, 193, 29  
 Albrecht, A., et al. 2006, *ArXiv Astrophysics e-prints*  
 Alcock, C., & Paczynski, B. 1979, *Nature*, 281, 358  
 Anderson, L., et al. 2014, *MNRAS*, 441, 24  
 Baldauf, T., Smith, R. E., Seljak, U., & Mandelbaum, R. 2010, *Phys. Rev. D*, 81, 063531  
 Bardeen, J. M., Bond, J. R., Kaiser, N., & Szalay, A. S. 1986, *ApJ*, 304, 15  
 Benson, B. A., et al. 2013, *ApJ*, 763, 147  
 Bernardeau, F., Colombi, S., Gaztañaga, E., & Scoccimarro, R. 2002, *Phys. Rep.*, 367, 1  
 Beutler, F., et al. 2012, *MNRAS*, 423, 3430  
 —. 2013, *ArXiv e-prints*  
 Blake, C., et al. 2011a, *MNRAS*, 418, 1707  
 —. 2011b, *MNRAS*, 415, 2892  
 Blanton, M. R., Lin, H., Lupton, R. H., Maley, F. M., Young, N., Zehavi, I., & Loveday, J. 2003, *AJ*, 125, 2276  
 Bolton, A. S., et al. 2012, *AJ*, 144, 144  
 Cacciato, M., van den Bosch, F. C., More, S., Li, R., Mo, H. J., & Yang, X. 2009, *MNRAS*, 394, 929  
 Cacciato, M., van den Bosch, F. C., More, S., Mo, H., & Yang, X. 2013a, *MNRAS*, 430, 767  
 Cacciato, M., van Uitert, E., & Hoekstra, H. 2013b, *ArXiv e-prints*  
 Chuang, C.-H., & Wang, Y. 2013, *MNRAS*, 435, 255  
 Chuang, C.-H., et al. 2013, *MNRAS*, 433, 3559  
 Cui, W., Borgani, S., Dolag, K., Murante, G., & Tornatore, L. 2012, *MNRAS*, 423, 2279  
 Das, S., et al. 2011, *ApJ*, 729, 62  
 Davis, M., Efstathiou, G., Frenk, C. S., & White, S. D. M. 1985, *ApJ*, 292, 371  
 Dawson, K. S., et al. 2013, *AJ*, 145, 10  
 de la Torre, S., et al. 2013, *A&A*, 557, A54  
 Doi, M., et al. 2010, *AJ*, 139, 1628  
 Eisenstein, D. J., et al. 2005, *ApJ*, 633, 560  
 —. 2011, *AJ*, 142, 72  
 Erben, T., et al. 2013, *MNRAS*, 433, 2545  
 Ettori, S., Donnarumma, A., Pointecouteau, E., Reiprich, T. H., Giodini, S., Lovisari, L., & Schmidt, R. W. 2013, *Space Sci. Rev.*, 177, 119  
 Feldman, H. A., Kaiser, N., & Peacock, J. A. 1994, *ApJ*, 426, 23  
 Foreman-Mackey, D., Hogg, D. W., Lang, D., & Goodman, J. 2013, *PASP*, 125, 306  
 Fukugita, M., Ichikawa, T., Gunn, J. E., Doi, M., Shimasaku, K., & Schneider, D. P. 1996, *AJ*, 111, 1748  
 Gao, L., & White, S. D. M. 2007, *MNRAS*, 377, L5  
 Gnedin, O. Y., Kravtsov, A. V., Klypin, A. A., & Nagai, D. 2004, *ApJ*, 616, 16  
 Goodman, J., & Weare, J. 2010, *Commun. Appl. Math. Comput. Sci.*, 5, 65  
 Gunn, J. E., et al. 1998, *AJ*, 116, 3040  
 —. 2006, *AJ*, 131, 2332  
 Guo, H., et al. 2013, *ApJ*, 767, 122  
 Guzik, J., & Seljak, U. 2001, *MNRAS*, 321, 439  
 Hajian, A., Battaglia, N., Spergel, D. N., Bond, J. R., Pfrommer, C., & Sievers, J. L. 2013, *JCAP*, 11, 64  
 Hasselfield, M., et al. 2013, *JCAP*, 7, 8  
 Hearin, A. P., & Watson, D. F. 2013, *MNRAS*, 435, 1313  
 Hearin, A. P., Watson, D. F., Becker, M. R., Reyes, R., Berlind, A. A., & Zentner, A. R. 2013, *ArXiv e-prints*  
 Heymans, C., et al. 2012, *MNRAS*, 427, 146  
 —. 2013, *MNRAS*, 432, 2433

- Hikage, C., Mandelbaum, R., Takada, M., & Spergel, D. N. 2013, MNRAS  
Hildebrandt, H., et al. 2012, MNRAS, 421, 2355  
Hill, J. C., & Spergel, D. N. 2014, JCAP, 2, 30  
Hinshaw, G., et al. 2013, ApJS, 208, 19  
Huff, E. M., Eifler, T., Hirata, C. M., Mandelbaum, R., Schlegel, D., & Seljak, U. 2014, MNRAS, 440, 1322  
Jing, Y. P., Mo, H. J., & Boerner, G. 1998, ApJ, 494, 1  
Kaiser, N. 1984, ApJ, 284, L9  
—, 1987, MNRAS, 227, 1  
Keisler, R., et al. 2011, ApJ, 743, 28  
Kravtsov, A. V., & Borgani, S. 2012, ARA&A, 50, 353  
Kroupa, P. 2001, MNRAS, 322, 231  
Lampeitl, H., et al. 2010, MNRAS, 401, 2331  
Landy, S. D., & Szalay, A. S. 1993, ApJ, 412, 64  
Leauthaud, A., et al. 2012, ApJ, 744, 159  
Li, C., Jing, Y. P., Mao, S., Han, J., Peng, Q., Yang, X., Mo, H. J., & van den Bosch, F. 2012, ApJ, 758, 50  
Lin, H., et al. 2012, ApJ, 761, 15  
Lupton, R., Gunn, J. E., Ivezić, Z., Knapp, G. R., & Kent, S. 2001, in Astronomical Society of the Pacific Conference Series, Vol. 238, Astronomical Data Analysis Software and Systems X, ed. F. R. Harnden, Jr., F. A. Primini, & H. E. Payne, 269  
Macciò, A. V., Dutton, A. A., & van den Bosch, F. C. 2008, MNRAS, 391, 1940  
Macciò, A. V., Dutton, A. A., van den Bosch, F. C., Moore, B., Potter, D., & Stadel, J. 2007, MNRAS, 378, 55  
Mandelbaum, R., Slosar, A., Baldauf, T., Seljak, U., Hirata, C. M., Nakajima, R., Reyes, R., & Smith, R. E. 2013, MNRAS, 432, 1544  
Mann, R. G., Peacock, J. A., & Heavens, A. F. 1998, MNRAS, 293, 209  
Mantz, A., Allen, S. W., Rapetti, D., & Ebeling, H. 2010, MNRAS, 406, 1759  
Maraston, C., et al. 2013, MNRAS  
Miller, L., et al. 2013, MNRAS, 429, 2858  
Miyatake, H., et al. 2013, ArXiv e-prints  
Mo, H. J., & White, S. D. M. 1996a, MNRAS, 282, 347  
—, 1996b, MNRAS, 282, 347  
More, S. 2011, ApJ, 741, 19  
—, 2013, ApJ, 777, L26  
More, S., van den Bosch, F. C., & Cacciato, M. 2009a, MNRAS, 392, 917  
More, S., van den Bosch, F. C., Cacciato, M., Mo, H. J., Yang, X., & Li, R. 2009b, MNRAS, 392, 801  
More, S., van den Bosch, F. C., Cacciato, M., More, A., Mo, H., & Yang, X. 2013, MNRAS, 430, 747  
More, S., van den Bosch, F. C., Cacciato, M., Skibba, R., Mo, H. J., & Yang, X. 2011, MNRAS, 410, 210  
Navarro, J. F., Frenk, C. S., & White, S. D. M. 1996, ApJ, 462, 563  
Norberg, P., Baugh, C. M., Gaztañaga, E., & Croton, D. J. 2009, MNRAS, 396, 19  
Norberg, P., et al. 2001, MNRAS, 328, 64  
Oguri, M., & Takada, M. 2011, Phys. Rev. D, 83, 023008  
Ostriker, J. P., Peebles, P. J. E., & Yahil, A. 1974, ApJ, 193, L1  
Padmanabhan, N., et al. 2008, ApJ, 674, 1217  
Peacock, J. A., & Smith, R. E. 2000, MNRAS, 318, 1144  
Percival, W. J., Cole, S., Eisenstein, D. J., Nichol, R. C., Peacock, J. A., Pope, A. C., & Szalay, A. S. 2007a, MNRAS, 381, 1053  
Percival, W. J., et al. 2004, MNRAS, 353, 1201  
—, 2007b, ApJ, 657, 645  
Perlmutter, S., et al. 1999, ApJ, 517, 565  
Pier, J. R., Munn, J. A., Hindsley, R. B., Hennessy, G. S., Kent, S. M., Lupton, R. H., & Ivezić, Ž. 2003, AJ, 125, 1559  
Planck Collaboration et al. 2013a, ArXiv e-prints  
—, 2013b, ArXiv e-prints  
—, 2013c, ArXiv e-prints  
—, 2013d, ArXiv e-prints  
—, 2013e, ArXiv e-prints  
Reddick, R., Tinker, J., Wechsler, R., & Lu, Y. 2013, ArXiv e-prints  
Reid, B. A., Seo, H.-J., Leauthaud, A., Tinker, J. L., & White, M. 2014, ArXiv e-prints  
Reid, B. A., & Spergel, D. N. 2009, ApJ, 698, 143  
Reid, B. A., et al. 2010, MNRAS, 404, 60  
Riess, A. G., et al. 1998, AJ, 116, 1009  
Ross, A. J., et al. 2012, MNRAS, 424, 564  
Rozo, E., et al. 2010, ApJ, 708, 645  
Rubin, V. C. 1983, Science, 220, 1339  
Rubin, V. C., Thonnard, N., & Ford, Jr., W. K. 1978, ApJ, 225, L107  
Rudd, D. H., Zentner, A. R., & Kravtsov, A. V. 2008, ApJ, 672, 19  
Samushia, L., Percival, W. J., & Raccanelli, A. 2012, MNRAS, 420, 2102  
Samushia, L., et al. 2014, MNRAS, 439, 3504  
Schlegel, D. J., Finkbeiner, D. P., & Davis, M. 1998, ApJ, 500, 525  
Scoccimarro, R., Sheth, R. K., Hui, L., & Jain, B. 2001, ApJ, 546, 20  
Seljak, U. 2000a, MNRAS, 318, 203  
—, 2000b, MNRAS, 318, 203  
Seljak, U., et al. 2005, Phys. Rev. D, 71, 043511  
Sheth, R. K., Mo, H. J., & Tormen, G. 2001, MNRAS, 323, 1  
Sheth, R. K., & Tormen, G. 1999, MNRAS, 308, 119  
Skibba, R. A., van den Bosch, F. C., Yang, X., More, S., Mo, H., & Fontanot, F. 2011, MNRAS, 410, 417  
Smee, S. A., et al. 2013, AJ, 146, 32  
Smith, J. A., et al. 2002, AJ, 123, 2121  
Spergel, D., Flauger, R., & Hlozek, R. 2013, ArXiv e-prints  
Springel, V., et al. 2005, Nature, 435, 629  
Sullivan, M., et al. 2011, ApJ, 737, 102  
Sunyaev, R. A., & Zeldovich, Y. B. 1972, Comments on Astrophysics and Space Physics, 4, 173  
Suzuki, N., et al. 2012, ApJ, 746, 85  
Takada, M., & Hu, W. 2013, Phys. Rev. D, 87, 123504  
Tegmark, M., et al. 2004, ApJ, 606, 702  
Tinker, J., Kravtsov, A. V., Klypin, A., Abazajian, K., Warren, M., Yepes, G., Gottlöber, S., & Holz, D. E. 2008, ApJ, 688, 709  
Tinker, J. L., Robertson, B. E., Kravtsov, A. V., Klypin, A., Warren, M. S., Yepes, G., & Gottlöber, S. 2010, ApJ, 724, 878  
Tinker, J. L., Weinberg, D. H., Zheng, Z., & Zehavi, I. 2005, ApJ, 631, 41  
van Daalen, M. P., Schaye, J., McCarthy, I. G., Booth, C. M., & Vecchia, C. D. 2014, MNRAS, 440, 2997  
van den Bosch, F. C., More, S., Cacciato, M., Mo, H., & Yang, X. 2013, MNRAS, 430, 725  
van den Bosch, F. C., Norberg, P., Mo, H. J., & Yang, X. 2004, MNRAS, 352, 1302  
Van Waerbeke, L., et al. 2000, A&A, 358, 30  
Velliscig, M., van Daalen, M. P., Schaye, J., McCarthy, I. G., Cacciato, M., Le Brun, A. M. C., & Dalla Vecchia, C. 2014, ArXiv e-prints  
Vikhlinin, A., et al. 2009, ApJ, 692, 1060  
Vogelsberger, M., et al. 2014, Nature, 509, 177  
White, M., et al. 2011, ApJ, 728, 126  
York, D. G., et al. 2000, AJ, 120, 1579  
Zaritsky, D., Smith, R., Frenk, C., & White, S. D. M. 1997, ApJ, 478, 39  
Zehavi, I., et al. 2011, ApJ, 736, 59  
Zentner, A. R., Hearin, A. P., & van den Bosch, F. C. 2013, ArXiv e-prints  
Zentner, A. R., Semboloni, E., Dodelson, S., Eifler, T., Krause, E., & Hearin, A. P. 2013, Phys. Rev. D, 87, 043509  
Zheng, Z., et al. 2005, ApJ, 633, 791